

MICROCOPY RESOLUTION TEST CHART
NATIONAL BUREAU OF STANDARDS-1963-A

DTIC FILE COPY

AD

4

AD-A190 757

CONTRACT REPORT BRL-CR-586

COMPUTATIONAL MODEL FOR
ARMOR PENETRATION
3RD ANNUAL REPORT

SRI INTERNATIONAL
333 RAVENSWOOD AVENUE
MENLO PARK, CA 94025

OCTOBER 1987

DTIC
SELECTED
FEB 24 1988
S D
E

APPROVED FOR PUBLIC RELEASE, DISTRIBUTION UNLIMITED

US ARMY BALLISTIC RESEARCH LABORATORY
ABERDEEN PROVING GROUND, MARYLAND

88 2 23 104

DESTRUCTION NOTICE

Destroy this report when it is no longer needed. DO NOT return it to the originator.

Additional copies of this report may be obtained from the National Technical Information Service, U.S. Department of Commerce, Springfield, VA 22161.

The findings of this report are not to be construed as an official Department of the Army position, unless so designated by other authorized documents.

The use of trade names or manufacturers' names in this report does not constitute indorsement of any commercial product.

REPORT DOCUMENTATION PAGE

Form Approved
OMB No 0704-0188
Exp Date Jun 30 1986

1a REPORT SECURITY CLASSIFICATION Unclassified		1b. RESTRICTIVE MARKINGS	
2a SECURITY CLASSIFICATION AUTHORITY		3. DISTRIBUTION/AVAILABILITY OF REPORT	
2b DECLASSIFICATION/DOWNGRADING SCHEDULE			
4 PERFORMING ORGANIZATION REPORT NUMBER(S) PYU 7893		5. MONITORING ORGANIZATION REPORT NUMBER(S)	
6a NAME OF PERFORMING ORGANIZATION SRI International	6b. OFFICE SYMBOL (if applicable)	7a. NAME OF MONITORING ORGANIZATION Ballistic Research Laboratory ATTN: SLCBR-TB	
6c ADDRESS (City, State, and ZIP Code) 333 Ravenswood Avenue Menlo Park, CA 94025		7b ADDRESS (City, State, and ZIP Code) Aberdeen Proving Ground, MD 21005-5066	
8a. NAME OF FUNDING/SPONSORING ORGANIZATION	8b OFFICE SYMBOL (if applicable)	9. PROCUREMENT INSTRUMENT IDENTIFICATION NUMBER DAAK11-78-C-0115	
8c. ADDRESS (City, State, and ZIP Code)		10. SOURCE OF FUNDING NUMBERS	
		PROGRAM ELEMENT NO.	PROJECT NO.
		TASK NO.	WORK UNIT ACCESSION NO.
11 TITLE (Include Security Classification) COMPUTATIONAL MODEL FOR ARMOR PENETRATION, 3rd Annual Report			
12 PERSONAL AUTHOR(S) D.C. Erlich, L. Seaman, T. Cooper, R.D. Caligiuri, and D.R. Curran (Project Supervisor)			
13a TYPE OF REPORT Contract Report	13b. TIME COVERED FROM <u>Oct 80</u> TO <u>Apr 83</u>	14 DATE OF REPORT (Year, Month, Day)	15 PAGE COUNT
16 SUPPLEMENTARY NOTATION			
17 COSATI CODES		18. SUBJECT TERMS (Continue on reverse if necessary and identify by block number)	
FIELD	GROUP	Armor Penetration, Shear Banding, Fragmentation, Computational Model, Depleted Uranium, RHA, Two-dimensional wave propagation code.	
11	06		
19	04		
19 ABSTRACT (Continue on reverse if necessary and identify by block number)			
<p>Results are reported for the third contractual year of a three - year experimental and analytical BRL/SRI International program to develop a computational capability for simulating armor penetration by projectile impact and for predicting the resultant downrange fragment environment. The baseline materials chosen for the experimental part of the program were rolled homogeneous armor (RHA) and depleted uranium alloy (DU) for the penetrator.</p> <p>Conclusions from previously performed armor penetration phenomenology studies involving the baseline materials (and 4340 steel, R_c 40) are reviewed, and the dominance of shear banding as the mechanism controlling both armor and penetrator erosion is reemphasized.</p> <p>Metallurgical analysis was performed on the DU alloy. The stress-strain flow curve was obtained from quasi-static tensile tests, and metallographic and fractographic</p>			
20 DISTRIBUTION/AVAILABILITY OF ABSTRACT <input checked="" type="checkbox"/> UNCLASSIFIED/UNLIMITED <input type="checkbox"/> SAME AS RPT <input type="checkbox"/> DTIC USERS		21 ABSTRACT SECURITY CLASSIFICATION Unclassified	
22a NAME OF RESPONSIBLE INDIVIDUAL Michael Scheidler		22b TELEPHONE (Include Area Code) 301/278-6836	22c OFFICE SYMBOL SLCBR-TB-W

19. ABSTRACT (con't)

examinations were made of both the as-received DU and DU specimens subjected to large dynamic shear deformations.

The contained fragmenting cylinder (CFC) technique for determining shear band kinetics parameters is reviewed and the shear band size distributions obtained from CFC experiments on both RHA and DU are presented. A preliminary set of RHA shear band kinetics parameters and a revised set of 4340 steel parameters were obtained for the modified SHEAR3 computational shear band model.

The development and testing of a two-dimensional wave propagation code (C-HEMP) particularly well-suited to armor penetration simulations has been largely completed. C-HEMP currently incorporates a complex slide line capability (for non-intersecting slide lines), a rezoner that handles large deformations, and the SHEAR3 model. C-HEMP with SHEAR3 was used to simulate previously performed armor penetration experiments, and C-HEMP correctly predicted the penetration and fragmentation phenomenology observed at impact velocities near and far above ballistic limit, although excessive cell distortion currently prevents complete simulations of deep penetration cases.

Details of the SHEAR3 model are presented in Volume 2.

Accession For	
NTIS CRA&I	<input checked="" type="checkbox"/>
DTIC TAB	<input type="checkbox"/>
Unannounced	<input type="checkbox"/>
Justification	
By	
Distribution/	
Availability Codes	
Dist	Avail and/or Special
AI	



EXECUTIVE SUMMARY

This is the first volume of a two-volume series comprising the third annual report for the program "Computational Model for Armor Penetration," performed by SRI International for the Ballistic Research Laboratory (Contract No. DAAK11-78-C-0115). The objective of the program was to develop a phenomenologically sound material disintegration model for computationally simulating armor penetration by projectile impact. The model would provide the capability to predict the ballistic limit and downrange fragment size and velocity distributions and would eventually be used by the DoD for armor and penetrator design. The materials studied in the program were 4340 steel (R_c40) and depleted uranium alloy, (DU) for the penetrators, and rolled homogeneous armor (RHA) for the target.

In Volume 1 we report on the experimental and analytical work performed during the third year to conclude the development of a computational model, SHEAR3, that describes the dominant material failure and fragmentation process (adiabatic shear banding) responsible for long-rod penetrator erosion and thick armor plate plugging and fragmentation. Volume 1 also describes application of SHEAR3 with the Lagrangian wave propagation code C-HEMP to computationally simulate penetration of armor plate by normally impacting long rods both near the ballistic limit and at higher velocities sufficient to produce significant back-of-the-armor fragmentation. (Remarks: both long rods and armor plate)

Volume 2 documents in detail the SHEAR3 model. (SHEAR3 model description)

In the following paragraphs we summarize both the third year results and the overall results of the three-year program.

Our effort to obtain material property data for calibrating the SHEAR3 model was completed this past year with the fractographic examinations, and contained fragmenting cylinder (CFC) experiments on

DU, and with the quantitative analysis of the CFC experiments on both DU and RHA to obtain shear band size distributions. Using these and previously determined results for 4340 steel, we performed a series of computational simulations of CFC experiments to obtain improved estimates of the SHEAR3 parameters for both RHA and 4340 steel.

The SHEAR3 subroutine must be used in a wave propagation hydrocode, and we have developed a code, C-HEMP, that is particularly well-suited for armor penetration calculations in which sophisticated failure models such as SHEAR3, must be used. During the third year of the program, C-HEMP was debugged, tested, and partially documented (see Volume 3).

Finally, SHEAR3 was used in C-HEMP to computationally simulate the normal impact of long 4340 steel rods into RHA plates at velocities ranging from near to well above the ballistic limit.

The status, after three years, of our attempt to understand and predict, in detail, armor penetration and disintegration based only on known material properties is as follows:

The observed behavior shows what appears, at first glance, to be an enormous variety of effects ranging from simple cratering and back surface bulging to plugging (see Figure 34, Volume 1) to penetration with catastrophic back-of-the-armor fragment sprays (see Figure 33, Volume 1). However, the first significant result of the program, reported in the first annual report, was that all the observed significant material failure and disintegration (erosion of the penetrator nose, plugging of the armor, and downrange fragmentation) were due to a single material failure mode, namely adiabatic shear banding. Thus, our modeling effort centered almost immediately on developing a model, SHEAR3, that is based on measurable laboratory material properties and that describes the nucleation, growth, and coalescence of adiabatic shear bands to form either one large fragment (the plug) or many small fragments (penetrator nose disintegration and erosion, as well as back-of-the-armor fragmentation).

For normal impact SHEAR3 appears to correctly predict penetrator nose erosion, the onset of plugging, and basic features of high velocity fragmentation correctly. However, excessive cell distortion prevents C-HEMP from carrying the calculation to completion for thick armor plates. Nonetheless, the calculated size distribution of the fragments surrounding the nose of the penetrator when the calculation halts is very similar to that observed experimentally for the downrange fragmentation, as reported in our second annual report.

The calculations have added significantly to our understanding of the penetration process, particularly the nature of the transitions from armor bulging to plugging to disintegration. These transitions proceed as follows.

At velocities approaching the ballistic limit, regions of completely shear banded material coalesce to form lobes that extend towards the rear of the armor plate; eventually, this material breaks out to form a plug (See Figures 38 and 37, Volume 1). A key feature of this process is that the impact velocity is below that of the propagation velocity for significant plastic strain levels. Thus, the back of the armor bulges as information about the impact reaches it. If shear banding were absent, this back surface bulge would be relatively smooth, but the shear banding causes localization of the strain at the incipient plug boundaries (See Figure 40, Volume 1). Thus, the ballistic limit is determined by the transition from bulging to plugging, and is caused by shear banding in lobes whose position is affected by the penetrator's communication with the rear of the armor plate. Simultaneously, the shear banding determines the penetrator nose erosion (see Figure 37, Volume 1).

At velocities well above the ballistic limit, another transition, occurs: from plugging to significant back-of-the-armor fragmentation. When the impact velocity exceeds the propagation velocity of significant plastic strain, the penetrator can no longer communicate with the rear of the armor plate, and much less bulging occurs. Thus, the large plastic deformation and associated material disintegration from

coalesced shear bands are confined within a "bow wave" around the eroding penetrator nose (see Figure 36 and compare with Figure 37). When this bow wave reaches the rear of the plate, a spray of fragments is released.

In summary, SHEAR3 in C-HEMP has significantly clarified our understanding of the penetration process for long rods impacting thick armor, and has given us the capability of studying the sensitivity of the ballistic limit and downrange fragmentation to changes in material properties. However, full use of this capability must await further development of C-HEMP to allow computational simulations of oblique impacts and of deeper penetrations. Recommendations for such further development are given in Chapter VI of Volume 1.

PREFACE

This report is Volume 1 of a two-volume series representing the third annual report on the program "Computational Model for Armor Penetration," performed by SRI International for Ballistic Research Laboratory (Contract No. DAAK11-78-C-0115). The titles and authors of the individual volumes in this series, as well as those of the previous annual reports for this program, are as follows:

<u>Title</u>	<u>Authors</u>
Vol. 1 - Computational Model for Armor Penetration	D. C. Erlich, L. Seaman, T. Cooper, D. R. Curran, and R. D. Caligiuri
Vol. 2 - Development of a Model for Shear Banding: SHEAR3	L. Seaman
First Annual Report - Computational Model for Armor Penetration	D. R. Curran, R. Burbach, R. D. Caligiuri, D. C. Erlich, L. Seaman, and D. A. Shockey
Second Annual Report - Computational Model for Armor Penetration	D. C. Erlich, L. Seaman, R. D. Caligiuri, and D. R. Curran

This program has benefited greatly from the technical support of Dr. Gerald Moss, the BRL project monitor, and Drs. Tim Wright and Richard Vitali of BRL.

The authors wish to acknowledge the excellent experimental and computational support at SRI International provided by A. Urweider, D. Henley, D. Petro, H. Hanna, B. Lew, and J. Kempf.

CONTENTS

PREFACE	vii
ILLUSTRATIONS	xi
TABLES	xv
I INTRODUCTION	1
Approach	2
Summary of Results Obtained During First Two Years of program	4
Outline of Recent Progress and Report Organization	6
II METALLURGICAL ANALYSIS OF DU	9
Quasistatic Tensile Test	9
Metallography	13
Fractography	15
Metallurgical Analysis of Du CFC Specimen	17
Summary of Results	20
III MATERIAL CHARACTERIZATION EXPERIMENTS	23
CFC Experiments with RHA	23
CFC Experiments with Du	37
Predictions from Critical Strain Theory	37
Qualitative Experimental Results	40
Anisotropy	45
Quantitative Damage Analysis	46
IV DETERMINATION OF SHEAR BAND KINETICS PARAMETERS FROM CFC EXPERIMENTS	51
CFC Data	51
Determination of Parameters	61
Fitting Procedure	64
V COMPUTER SIMULATION OF ARMOR PENETRATION.....	67

CONTENTS (Continued)

VI	RECOMMENDATIONS FOR FUTURE WORK	83
	Task 1: Refinements to Shear Band Model	84
	Task 2: Improvements to C-HEMP for Armor Penetration Calculations	86
	Task 3: Proof Tests of the Computational Method	92
	Task 4: Simplification of Computational Method	94
	Task 5: Application of Computational Method to Various Scenarios	97
	Task 6: Documentation and Transfer to BRL	98
	REFERENCES	99
	DISTRIBUTION LIST	103

ILLUSTRATIONS

1	Measured Stress-Strain Curve of DU-3/4 Ti Alloy	11
2	Microstructure of DU-3/4 Ti Alloy	14
3	Fracture Surface of DU-3/4 Ti Alloy	16
4	Detail of Fracture Surface of DU-3/4 Ti Alloy, Showing Large Steps, Secondary Cracks, and Dimples	16
5	U ² Ti Inclusion and Ductile Dimples on Fracture Surface of DU-3/4 Ti Alloy	18
6	Microstructure of DU-3/4 Ti Alloy Cylinder After Expansion	19
7	Schematic of CFC Experiments for Studying Shear Band Kinetics	24
8	Geometry and Nomenclature for Shear Bands in Fragmenting Cylinder Experiments	25
9	Cross Section of RHA CFC Experiments	26
10	CFC Specimens Machined from RHA Slab, Showing Mode I Shear Bands in Planes Perpendicular to Rolling Plane	29
11	Two Views of Half of the RHA Specimen Tube L-4 Recovered from CFC Experiment	30
12	Polished and Etched Section Through RHA Specimen L-4, Showing Preponderance of Shear Banding Damage in Rolling Direction	31
13	Two Views of Half of the RHA Specimen T-7 Recovered From CFC Experiment	32
14	Half of RHA Specimens T-9 and T-10 Recovered from CFC Experiments	33
15	Cumulative Size Distributions of Shear Bands from RHA Shot T-7	34

ILLUSTRATIONS (Continued)

16	Cumulative Size Distributions of Shear Bands from RHA Shot T-9	35
17	Cumulative Size Distributions of Shear Bands from RHA Shot T-10	36
18	Cross Section of DU CFC Experimental Apparatus	38
19	Sliced DU Tubes Recovered from CFC Experiments	42
20	Transverse Slice near Midaxial Plane of a Portion of DU Specimen Recovered from CFC Shot 11	43
21	Two Shear Bands in DU	45
22	Inside Surface of Shear Band-Damaged End of Half of DU Tube Recovered from CFC Shot 12	48
23	Cumulative Size Distributions of Shear Bands from DU Shot 12	49
24	Cross Section of 4340 Steel (R_c40) CFC Experiments	52
25	Calculated Plastic Strain Histories for RHA Test T-2	54
26	Calculated Plastic Strain Histories for RHA Test T-9	55
27	Calculated Plastic Strain Histories for RHA T-10	56
28	Calculated Plastic Strain Histories for 4340 Steel Test 2	57
29	Calculated Plastic Strain Histories for 4340 Steel Test 8	58
30	Calculated Plastic Strain Rate Histories for RHA Test T-9	59
31	Calculated Plastic Strain Rate Versus Strain for RHA Test T-9	60
32	Cross-Sectional Geometry for Penetration Simulations	66
33	Radiographs Taken 30, 145, and 285 μ s After 1.55 km/s Impact of a 4340 Steel (R_c40) Rod onto an RHA Plate	69

ILLUSTRATIONS (Continued)

34	Cross Sections Through Centers of RHA Targets Impacted by 4340 Steel ($R_c 40$) Projectiles	70
35	Portion of Initial Cell Layout for Penetration Simulations	71
36	Profile of Simulation No. 1 ($V_1 = 1550$ m/s) 11.1 μ s After Impact	73
37	Profile of Simulation No. 3 ($V_1 = 750$ m/s) 12.3 μ s After Impact	75
38	Profile of Simulation No. 5 ($V_1 = 500$ m/s) 12.5 μ s After Impact	77
39	Effect of Shear Banding Damage on Simulated Penetration at an Impact Velocity of 1550 m/s	79
40	Effect of Shear Banding Damage on Simulated Penetration at an Impact Velocity of 750 m/s	80
41	Initial Cell Profiles for SWE2D Deep Penetration Simulation, Using a Combination of Triangular and Quadrilateral Cells	88
42	Computational Profile 30 μ s After Start of SWE2D Deep Penetration Simulation, and Detail of Highly Deformed Region	89

TABLES

1	Summary of Quasi-Static Tensile Test Results On DU-3/4 Ti Alloy.....	11
2	Parameters and Qualitative Results for RHA CFC Experiments	27
3	Parameters and Qualitative Results for DU CFC Experiments	39
4	Critical Strains for Shear Band Initiation in Various Materials, as Calculated from Equation (1), and Material Parameters Used in The Calculations	41
5	Shear Band Damage Characterization Parameters for RHA and 4340 Steel from CFC Data and C-HEMP Simulations	62
6	Shear Banding Kinetics Parameters in SHEAR3	63
7	SHEAR3 and EP Model Parameters	66
8	C-HEMP Penetration Simulations	70

I INTRODUCTION

The traditional empirical approach for designing armor and penetrator systems has often been effective in gaining successive incremental improvements over the established state of the art. However, as more complex systems are introduced, the very lengthy and expensive empirical approach becomes less and less tractable. Recently developed computational methods can now handle complex shapes, deformations, and material behavior and are therefore more likely to be effective in streamlining armor and penetrator design.

The computational approach to armor and penetrator design is an iterative procedure beginning with approximate computer simulations of a penetration scenario, using existing simple models for material behavior and estimated values of material properties. Test firings are then performed to evaluate the performance of the design, to provide data for comparison with the calculated results, and to indicate the adequacy of the material behavior models and material property values. The test results suggest changes in the design and guide the selection and development of dynamic material property tests and improved material behavior models for the next series of computer simulations. Test firings of a second generation design are then performed, and the results are compared with the computational results, as before.

The procedure is repeated until the system attains the desired performance. This approach, currently being developed by DoD, reduces the overall design effort because the interaction of experiments and calculations lead more rapidly to an acceptable design than a purely empirical approach.

Computer simulation of armor penetration must model the following material behavior: a thermodynamic equation of state, the plastic flow, and the material disintegration. Existing thermodynamic equation of state models are adequate for most armor penetration calculations, as

are existing models for plasticity (although material property values related to plasticity at high strain rates are often lacking). The greatest weakness is in the modeling of the material disintegration,¹ which can occur by several mechanisms, depending on the material, temperature, stress, strain, and strain rate. Of the three principle failure modes occurring at high loading rates--brittle fracture, ductile fracture, and shear banding--the last two have been most commonly observed in connection with metallic armor.

Simple, empirically derived failure criteria may provide some predictive capability for penetration scenarios within a very specific range of geometries and impact velocities. However, a generalized failure model applicable to a wide range of scenarios requires a detailed qualitative and quantitative understanding of the material disintegration processes involved, specifically the nucleation, growth, and coalescence of brittle cracks, ductile voids, and shear bands.

Considerable work has been performed in studying and modeling some of these material disintegration models. SRI International has developed the nucleation and growth (NAG) Micro-Statistical Fracture Mechanics (MSFM) models for brittle and ductile dynamic tensile failure, which have proven quite useful as predictive models.²⁻¹⁰ Before this program, some work had been done in studying and formulating a preliminary model for failure by the nucleation, growth, and coalescence of shear bands.¹¹⁻¹⁴ However, no method existed that would incorporate these models into a computer code that would simulate the penetration of armor by projectile impact and predict the resulting fragmentation environment.

Approach

The objective of this program was to develop a phenomenologically sound material disintegration model for computationally simulating armor penetration by projectile impact. This model would provide the capability for predicting the downrange fragment size and velocity distributions and would eventually be used by the DoD for armor and penetrator design.

Our approach for this program is described below.

Baseline materials--depleted uranium (DU)-3/4 wt% titanium alloy and rolled homogeneous armor (RHA)--were procured and metallurgically analyzed. Penetration phenomenology experiments were performed, using various impact geometries, velocities, and obliquities, and the recovered projectile and target specimens were sectioned and examined metallographically to reveal the key microstructural damage mechanisms that govern the failure and disintegration of both the penetrator and the armor. A previously acquired data base was available for 4340 steel.

Characterization experiments were performed that exercised a particular failure mechanism in a geometry that is relatively simple to simulate computationally. These experiments provided a basis for developing or refining a failure model and generating material failure kinetics parameters. The contained fragmenting cylinder (CFC) test, for example, was used to study shear band nucleation and growth.

Computational models were developed to describe the observed failure mechanisms. The models were based upon the NAG MSFM models, which attempt to qualitatively and quantitatively simulate the actual micromechanical failure processes involved.

Material failure kinetics parameters were determined by computationally simulating the material characterization experiments, using the failure model to describe the damage. The parameters were then used to predict damage in scenarios with different geometries or loading conditions.

A computer code (C-HEMP) was assembled, containing the features necessary to simulate armor penetration by projectile impact. Although this code includes many of the same features found in various HEMP codes, it also contains new logic to handle the complex phenomenology observed and to incorporate the material failure models developed above.

Finally, computer simulations were performed to assess the ability of the computational method to correctly predict the main features of armor penetration.

These six parts to our approach for this program were not performed sequentially, but proceeded simultaneously with much interaction and iteration between them.

Summary of Results Obtained During First Two Years of Program

Details of the results obtained during the first two years of the program are available in the first and second annual reports.^{15,16} Those results are summarized below.

The two baseline materials, RHA and a DU alloy, were obtained, and RHA was examined metallurgically. Quasi-static tensile tests were performed on RHA specimens that were cut along three orthogonal directions. The resulting stress-strain flow curves revealed a significant anisotropy in ductility.

We studied the phenomenology of high-velocity penetration of moderate-to-thick armor plate by long-rod projectiles using both new and existing quarter- and full-scale ballistics data for DU (and 4340 steel) projectiles impacting RHA targets at velocities both near and well above the ballistic limit, and at obliquities from zero to seventy degrees. We drew the following conclusions from these studies:

- (1) Shear banding is the dominant failure mechanism in both the penetrator and the target, and the coalescence of shear bands form the bulk of the downrange and uprange fragments.
- (2) Shear-band-induced penetrator backflow and shear failure along planes of weakness in an anisotropic target are significant mechanisms of target erosion.
- (3) Tensile failure may be a factor, but only in a relatively few instances, such as at the rear of the armor plate in the final stages of penetration for an impact velocity just above the ballistic limit.

- (4) Projectiles change direction within the target (oblique impacts only) seeking the path of least resistance.
- (5) Most of the failure mechanisms in a highly oblique impact will also be found in a normal impact of the same materials at the same velocity.

From these phenomenological conclusions, we selected the failure mechanisms to be studied in detail and the features that would be needed for a predictive computer code. We decided that shear band kinetics parameters are crucial for both the penetrator and target, while tensile failure parameters are relatively unimportant, particularly for the penetrator. Furthermore, the computer code would need features that could handle the extreme shear deformations (a rezoner), the rotation of a projectile in an oblique impact (self-directed or wandering slide line), and anisotropic shear failure. Finally, simulations of normal impacts, which are easier to perform than those of oblique impacts (because of the axial symmetry), are valid tests of the computational model's ability to predict fragmentation distributions.

To measure the kinetics of the shear banding process, we performed (CFC) experiments with RHA specimens cut along two orthogonal directions. The experiments yielded a wide range of shear banding damage and confirmed the expected significant anisotropy in shear banding. At the same time, computational model for shear banding in an isotropic material (SHEAR3) was developed and calibrated with respect to previously obtained CFC data on 4340 steel, and the shear band kinetics parameters for 4340 steel (R_c40) were obtained.

A quarter-scale armor penetration test was performed at BRL to provide a back-of-the-armor fragmentation data base using materials (RHA and 4340 steel, R_c40) for which data on shear band kinetics existed. Preliminary simulations of this test were made using the SHEAR3 model (but with only rough estimates of the RHA shear band kinetics parameters) and an existing two-dimensional code, TROTT. Although the simulations would not run to completion (because TROTT could not handle the large shear deformations), the calculated size distributions of fragments resulting from shear banding damage were in fair agreement

with experimental observations, indicating that a phenomenologically based failure model, which describes fragmentation as the nucleation, growth, and coalescence of shear bands, has a good potential for predictive capabilities.

A search was made for a two-dimensional wave propagation code that had all or most of the computational features that had been seen, from the phenomenology study described above, to be important in simulating armor penetration by projectile impact. These computational features included a finite-element cell numbering scheme (to allow for material ejection and for the inclusion of slide lines in arbitrary directions after a calculation has begun), an advanced slide line capability (including intersecting and wandering slide lines), a rezoning feature that can account for extreme cell distortions, and the ability to handle the complex failure models. When this search turned up no viable candidates, work was begun to formulate, assemble, and test a code incorporating many of these features, with the potential for adding the remaining features at a later time. This code was called C-HEMP (short for Composite HEMP), because it was largely a composite of several HEMP-type codes.

Outline of Recent Progress and Report Organization

In this section we will briefly outline the progress made in this program since the second annual report and describe the organization of this three-volume report.

The experimental work planned for this program has been completed. A metallurgical analysis was performed on the baseline DU alloy. Quasi-static tensile tests yielded a stress-strain flow curve, and the DU specimens recovered from these tests and a CFC test were subjected to metallographic and fractographic examination. These results are discussed in Section II of Volume I.

Quantitative analysis was completed on the RHA CFC experiments performed during the first and second years of the program, and shear band size distributions were obtained. A series of DU CFC experiments

was performed and analyzed, and the shear band size distributions were obtained. The results are shown in Section III of Volume I, along with a brief review of the CFC technique.

Refinements were made to the SHEAR3 computational model for shear banding damage in isotropic materials. These included a more explicit strain rate dependence for shear band nucleation. Complete documentation for this model is in Volume II of this report. Work was begun to develop a significantly more complex model for shear banding in anisotropic materials (SHEAR4), but limitations on the scope of this program did not allow this work to be completed. A discussion of some of the features of SHEAR4 is included in Section VI of Volume I.

The modified version of SHEAR3 was used (in conjunction with C-HEMP) to simulate the RHA CFC experiments, to obtain a preliminary set of shear band kinetics parameters for RHA, and to obtain a revised set of parameters for 4340 steel (R_c40). The results are shown in Section IV of Volume I.

The development and testing of the C-HEMP code is nearly complete. Incorporated features that have proven successful in a several different applications include a free-field input format, a finite-element cell numbering scheme, a rezoner, a reasonably complex slide line routine (including slip, with or without a frictional component, along user-located single or intersecting slide lines that are either already "unzipped" or "unzip" as the calculation proceeds), and the inclusion of the SHEAR3 and elastic-plastic equation-of-state subroutines. Complete documentation of C-HEMP will be available later.

A series of computational simulations of armor penetration was performed with C-HEMP, to test the various features of the new code.

These simulations of the normal impact of a 4340 steel projectile into an RHA armor plate demonstrate, at least in a preliminary way, the ability of C-HEMP and SHEAR3 to realistically model armor penetration both near and well above the ballistic limit. This work appears in Section V of Volume I.

Finally, we have written a detailed set of recommendations for future work in the area of computational modeling of armor penetration. This appears in Section VI of Volume I.

II METALLURGICAL ANALYSIS OF DU

Computational modeling of the large deformations and material failure that accompany the penetration of an armor plate by a projectile requires knowing the constitutive behavior of the materials involved and identifying the microstructural mechanisms leading to fracture. Much of this information can be provided by quasi-static tensile tests and metallographic and fractographic observations of the tensile specimens.

Metallurgical studies of the baseline armor material, RHA, conducted during the first year of the program, have been previously reported.¹⁵ Similar studies were performed during the final year of the program on the baseline penetrator material, a DU-3/4Ti alloy. In this section, we will discuss the results of these studies and a further metallurgical study of a DU specimen recovered from a CFC experiment.

Quasistatic Tensile Tests

Smooth round-bar tensile specimens were machined by the Rocky Flats Plant of Rockwell International in Golden, CO, from extruded and heat-treated rods of a single heat of DU-3/4Ti alloy. Three sets of specimens were prepared in accordance with specifications provided by SRI. The first set of specimens had a 2.5-cm gage length, a 0.625-cm gage diameter, and was machined with the axes parallel to the extrusion direction (longitudinal specimens). The second set had a 1.27-cm gage length, a 0.32-cm diameter, and was also machined with the axes perpendicular to the extrusion direction and intersecting the rod centerline (transverse specimens). The third set had a 0.51-cm gage length, a 0.32-cm gage diameter, and was also machined in the transverse direction, but not intersecting the rod centerline (microtensile specimens).

This last set was for the purpose of assessing the affect of any centerline porosity on the tensile properties of the extruded rods.*

Two longitudinal and two transverse tensile specimens were pulled to fracture, using an Instron testing machine at a crosshead speed of 8×10^{-4} cm/s. The results of these tests are summarized in Table 1 and the corresponding true stress-true strain curves are shown in Figure 1.

The results show that in the the DU alloy is somewhat weaker in the transverse direction than in the longitudinal direction. For transverse directions the yield stress is about 7.6 kbar (110 ksi) and true fracture stress is about 15 kbar (218 ksi), as compared to 9.0 kbar (130 ksi) and 16.2 kbar (235 ksi), respectively, for the longitudinal specimens. On the other hand, the ductility is about the same for both specimen orientations, considering the scatter in the elongation and fracture strain data. This observation is consistent with the literature on the dependence of fracture toughness on orientation for extruded DU-3/4Ti.¹ From these results, we concluded that any centerline porosity that might exist is not important to the mechanical properties of these rods, and therefore testing of the microtensile specimens was unnecessary.

The post-yield data in Figure 1 may be described by a power law hardening equation of the form:

$$\sigma = k\epsilon^n$$

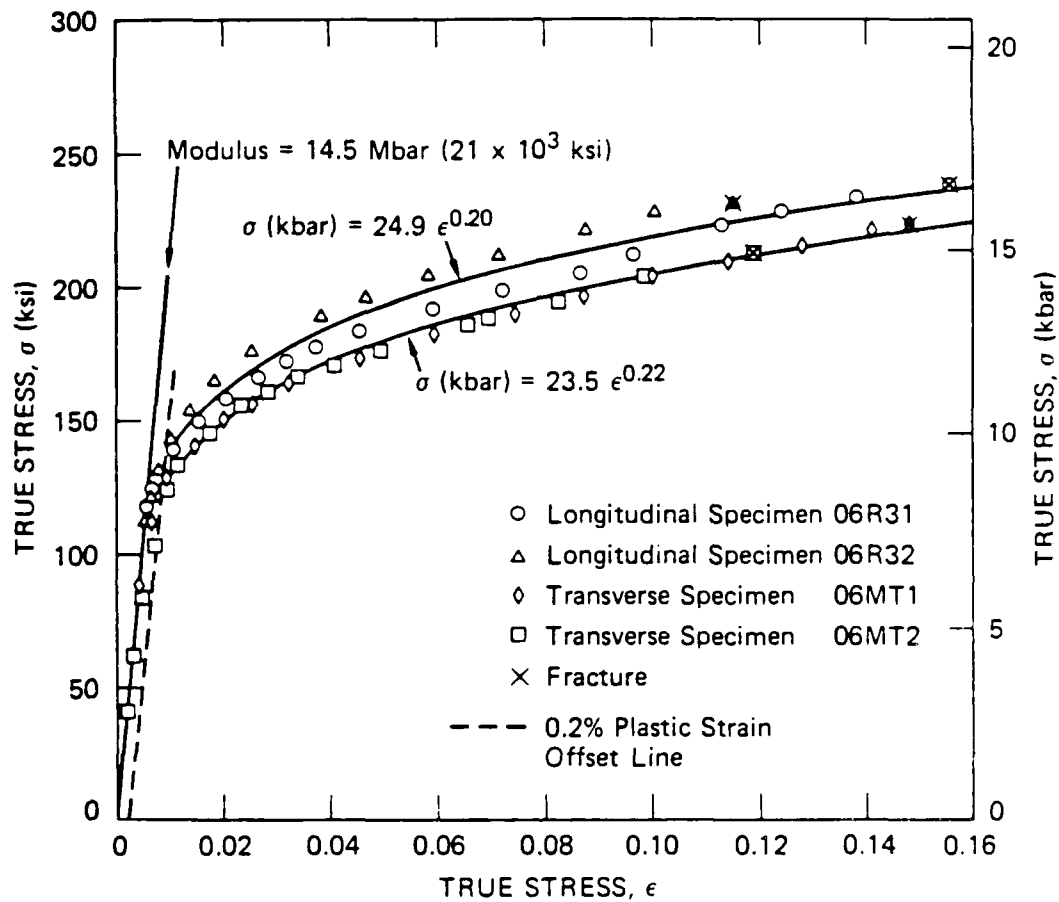
where $k = 24.9$ kbar (236 ksi) and $n = 0.20$ for the longitudinal data, and $k = 23.5$ kbar (234 ksi) and $n = 0.22$ for the transverse data.

*Centerline microporosity has been a chronic problem in the extrusion of uranium alloys. Although the pores are often quite small (smaller than the detection limit of x-rays), they have the potential for influencing material properties of extruded products. The cause of such porosity is not well established.

Table 1

SUMMARY OF QUASI-STATIC TENSILE TEST RESULTS ON DU-3/4 Ti ALLOY

Specimen Number	Yield stress (0.2% Offset)		True Stress at Fracture		True Strain at Fracture	Elongation to Failure (%)
	kbar	ksi	kbar	ksi		
Longitudinal						
06R31	8.97	130	16.5	239	0.155	17
06R32	8.97	130	15.9	231	0.115	12
Transverse						
06MT1	7.73	112	15.4	223	0.148	16
06MT2	7.45	108	14.7	213	0.119	14



MA-7893-139A

FIGURE 1 MEASURED STRESS-STRAIN CURVE OF DU-3/4 Ti ALLOY

These minor differences in work-hardening parameters are most likely due to microstructural texturing effects during the extrusion process.

Metallography

The broken halves of one longitudinal and one transverse DU tensile specimen were sectioned along their axis, ground, and electropolished for metallographic examination. Figure 2 is a micrograph from the longitudinal specimen. The needle-like character of the microstructure is due to the martensitic (diffusionless) transformation of the high temperature q-phase (BCC) into the a-phase (orthorhombic) upon quenching. The as-quenched structure is not equilibrium a-phase, but is rather a slightly distorted orthorhombic structure termed a'. The q grain structure generated during the solutionizing treatment is still faintly visible in Figure 2. The q grain size is estimated to have been on the order of 0.1 to 0.5 mm.

The martensitic transformation of q uranium into the metastable structure did not strengthen the material (as it would in steel); it is simply a mechanism to achieve a supersaturated uranium-titanium solid solution. The material was strengthened by a subsequent aging treatment at 360°C, as will be discussed below. It is evident from Figure 2 that this aging treatment did not substantially alter the acicular morphology of the a' grains, suggesting that only a small amount of the metastable a' converted to equilibrium a during aging. Although not visible in Figure 2, patches of equilibrium a were occasionally observed along the a grain boundaries.

Note also from Figure 2 that the alloy contains many large (approximately 10 μm across) precipitates. Energy-dispersive x-ray analysis indicates that these precipitates are Ti rich, and probably consist of the intermetallic compound U_2Ti . In longitudinal cross sections--that is, in planes containing the rod axis--these precipitates are in ordered long stringers parallel to the extrusion direction. In transverse cross sections, the precipitate distribution is random. Therefore, these precipitates form either during cooling from the homogenizing temperature prior to extrusion or during the extrusion process itself.



MP-7893-140

FIGURE 2 MICROSTRUCTURE OF Du-3/4 Ti ALLOY
(Polarized Light)

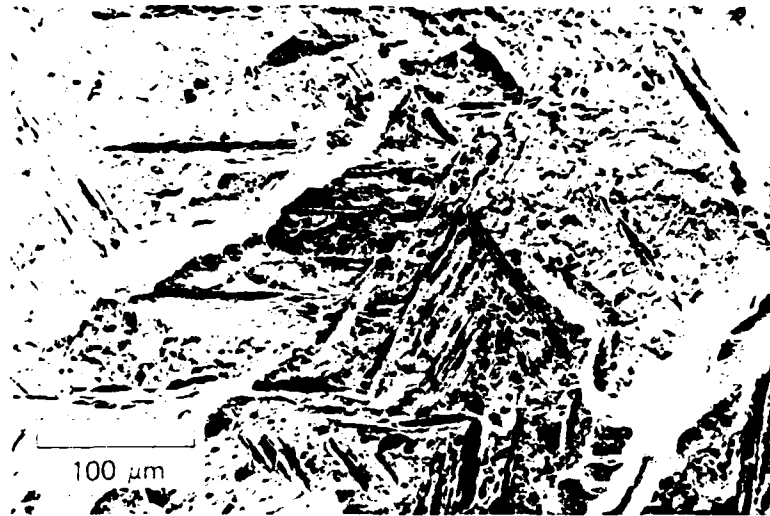
In addition to these large unintentional precipitates, there is a uniform distribution of very fine ($\ll 1 \mu\text{m}$ across) U_2Ti particles, not resolvable by optical microscopy.¹⁷ These particles are produced by aging the solutionized and quenched extruded rod at 360°C for several hours, and they inhibit the motion of dislocations through the lattice. Therefore, a higher stress is needed to move the dislocations past these precipitates, increasing the yield strength of the material.

Examination of the cross sections of the broken tensile specimens did not reveal any microcracking or void growth below the fracture plane. Furthermore, all the specimens failed before any significant necking occurred. However, the second longitudinal specimen (O6R32 in Figure 1) did display an interesting feature: a secondary crack formed perpendicular to the axis and about 0.5 cm below the main fracture plane. This crack propagated through 95% of the cross section before arresting.

Fractography

The fracture surfaces of a longitudinal and transverse DU tensile specimen were studied with scanning electron microscopy. In both cases, the surface was a mixture of transgranular and dimple fracture as has been observed in the literature.¹⁸ The surface topology of a representative longitudinal specimen is illustrated in Figures 3 and 4. Figure 3 shows large steps in the fracture surface running from bottom left to top right across the fractograph. The darker featherlike features are the martensitic needles seen previously. Figure 4 shows a detail of one of the steps in the fracture surface, with secondary cracks running parallel to the cleavage plane. Note also the network of dimples surrounding the transgranular fracture.

Several large globular U_2Ti precipitates are also visible in Figure 3. While these precipitates are too large to affect the yield strength, they definitely contribute to the ultimate tensile fracture process and lower the overall ductility.



MP-7893-141

FIGURE 3 FRACTURE SURFACE OF Du-3.4 Ti ALLOY



MP-7893-142

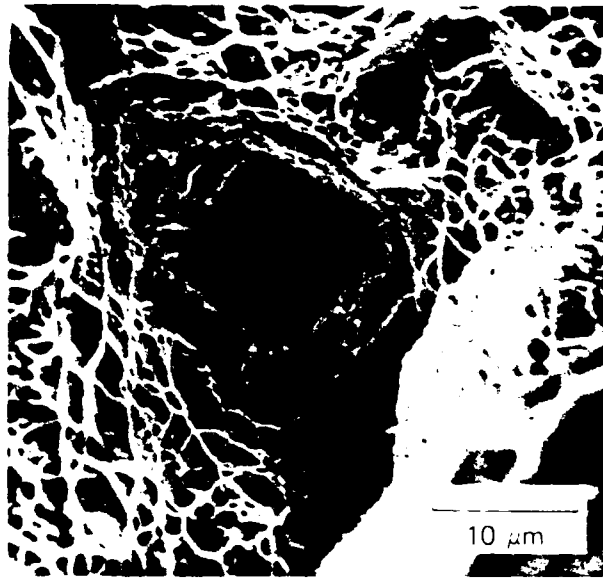
FIGURE 4 DETAIL OF FRACTURE SURFACE OF DU-3.4 Ti ALLOY SHOWING LARGE STEP, SECONDARY CRACKS, AND DIMPLES

The only difference between the fracture surface of the longitudinal and transverse specimens is the already mentioned difference in the large precipitate distribution. On the fracture surface (which is perpendicular to the cross sections used for metallographic observations), the precipitate distribution is random for the longitudinal specimens, whereas long ordered stringers are seen in the transverse specimens. A typical large U_2Ti precipitate is shown in Figure 5. It has a characteristic cubic shape and is about 10 μm in across. The matrix- U_2Ti interface is apparently stronger than the U_2Ti , and thus in most cases the inclusions fracture rather than debond.

Metallurgical Analysis of DU CFC Specimen

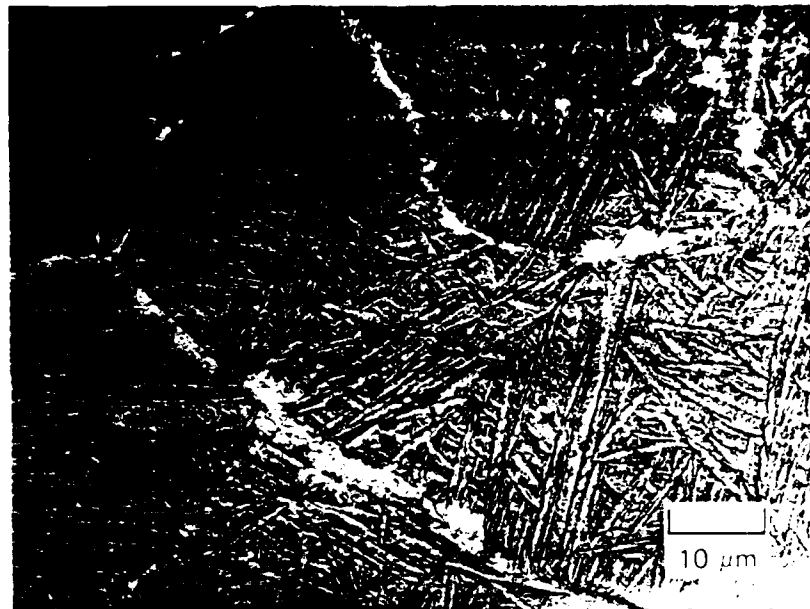
As will be discussed in detail in Section III, we performed a series of DU CFC experiments to study shear banding kinetics in DU. The CFC specimens were cylindrical tubes machined from extruded rod from the same heat used for the tensile specimens, and were thermomechanically processed in a similar manner. We metallurgically examined a DU specimen recovered from one of these experiments to determine if the explosively driven deformation and heating that accompany a CFC experiment caused any significant microstructural changes in the material.

The microstructure of the recovered DU CFC fragment, as shown in Figure 6(a), is primarily acicular α' , the martensitic form of the equilibrium orthorhombic ($\alpha-U$) structure. This martensitic form, produced by rapidly quenching U-Ti alloys from the BCC (γ) phases, is also orthorhombic, but with a shortened b axis.¹⁹ The prior γ grain boundaries, clearly visible in Figure 6(a), are the result of the pre-quench soaking treatment at temperatures higher than 750°C.²⁰ During quenching, the α' platelets initiate from the γ grain boundaries and propagate rapidly across the grains, thereby marking the locations of these grain boundaries. This is essentially the same microstructure as observed for the tensile specimens.

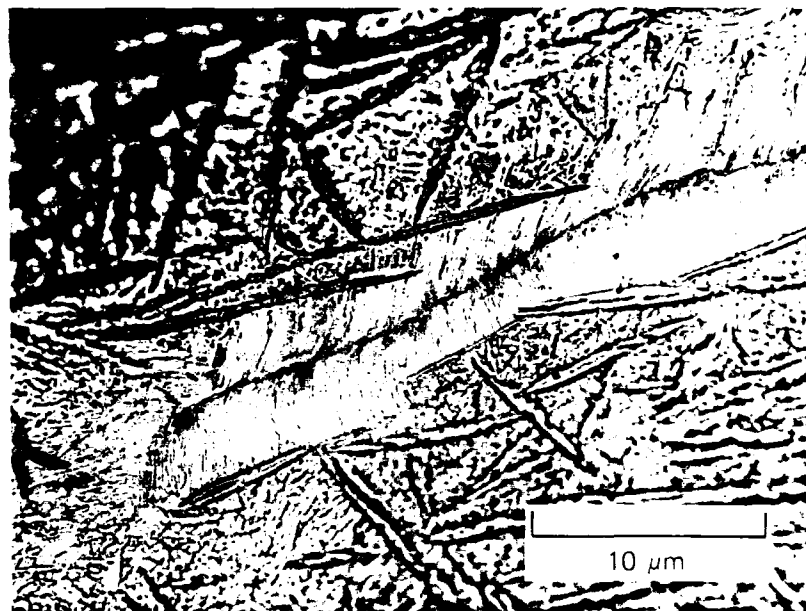


MP-7893-143

FIGURE 5 U₂Ti INCLUSION AND DUCTILE DIMPLES
ON FRACTURE SURFACE OF DU-3/4 Ti
ALLOY



(a)



(b)

MP-7893-158

FIGURE 6 MICROSTRUCTURE OF DU-3.4 Ti ALLOY CYLINDER AFTER EXPANSION

(a) shows the α -uranium martensite needles, the prior γ grain boundaries, and the α -uranium plus U_2Ti formed on the prior γ boundaries as a result of over-aging.

(b) shows the lamellar structure of the α -uranium plus U_2Ti formed on the prior γ boundaries.

Note also in Figure 6(a) the white material found predominantly along the prior γ grain boundaries. This material is the equilibrium α -U/U₂Ti structure and is a result of overaging.²¹ During prolonged aging treatments, the equilibrium structure nucleates along the prior boundaries and then grows into the matrix. If held long enough at temperature,* the entire microstructure would revert to the equilibrium structure of α -U/U₂Ti. As shown in Figure 6(b), this equilibrium structure initially exhibits a lamellar morphology with alternating layers of α -U and U₂Ti. If held for very long times at temperature, the U₂Ti platelets will eventually become spheroid to minimize the free energy of the system.

Since both the acicular α' structure and the equilibrium α -U/U₂Ti structure were found in the quasi-static tensile specimens, we concluded that the shock loading and subsequent heating did not substantially alter the microstructure. To confirm this we performed a series of hardness tests across the thickness of the recovered fragment and measured a hardness of 395 ± 16 VHN. This differed negligibly from the 388 ± 26 VHN hardness measured in the as-received specimens. It therefore appears that the CFC experiment does not cause any significant microstructural changes that may influence the initiation or propagation of adiabatic shear bands.

Summary of Results

The DU-3/4Ti alloy from extruded rod, which was tested for this program, has the following tensile properties:

yield stress -- 7.4-9.0 kbar (108-130 ksi)
true fracture stress -- 14.7-16.5 kbar (213-239 ksi)
true fracture strain -- 12-16%

*Unlike the martensitic $\alpha \rightarrow \alpha'$ transformation, the $\alpha' \rightarrow \alpha$ transformation is diffusion controlled.

Relatively little anisotropy in tensile properties was observed between longitudinal and transverse directions.

The DU alloy has an acicular α' microstructure with a nonuniform distribution of large U_2Ti precipitates. Fracture occurs by a mixture of cleavage and dimple rupture, with cleavage as the dominant mode.

No significant microstructural changes were found in rapidly deformed specimens, before initiation of shear banding.

III MATERIAL CHARACTERIZATION EXPERIMENTS

During this program, we performed two series of CFC experiments, one with RHA and one with DU. The purpose of these experiments was to measure the shear band size and density distributions in specimens that underwent a readily characterized strain history, and determine from this data the shear banding kinetics parameters.

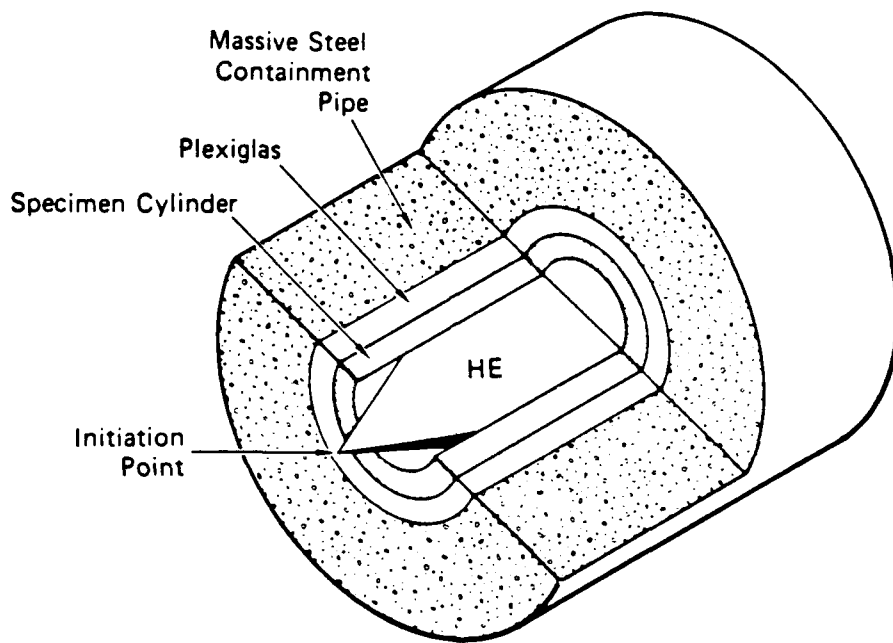
We have previously reported¹⁵⁻¹⁶ details of the experimental technique and the analytical method for obtaining shear band kinetics parameters from the experimental data (as was performed last year for 4340 steel, $R_c 40$). In this section we will, after a brief review of the CFC technique, present the results of the CFC experiments on RHA and DU.

The CFC technique consists of applying internal explosive loads to thick-walled cylinders of the specimen material so that they expand rapidly until stopped by massive concentric containment cylinders. The setup is shown schematically in Figure 7. The initial deformation rate and the final deformation achieved are controlled by the explosive density and the thicknesses of the various containment cylinders. Mode I shear bands (see Figure 8) originating at the inner surface of the recovered specimen tube are measured and counted, and the resulting shear band size distributions as a function of axial position along the tube are correlated with those obtained from computer simulations to determine the shear banding kinetics parameters.

CFC Experiments with RHA

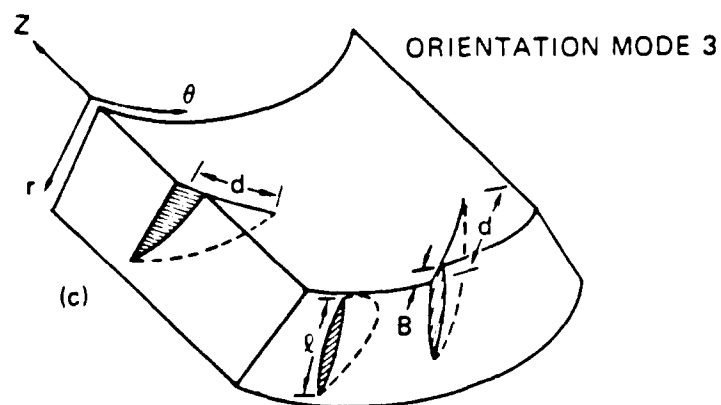
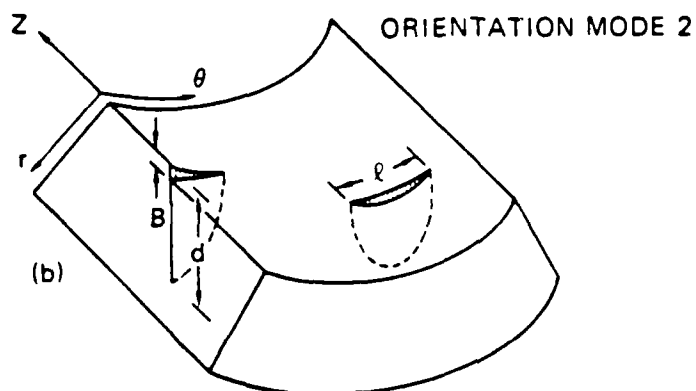
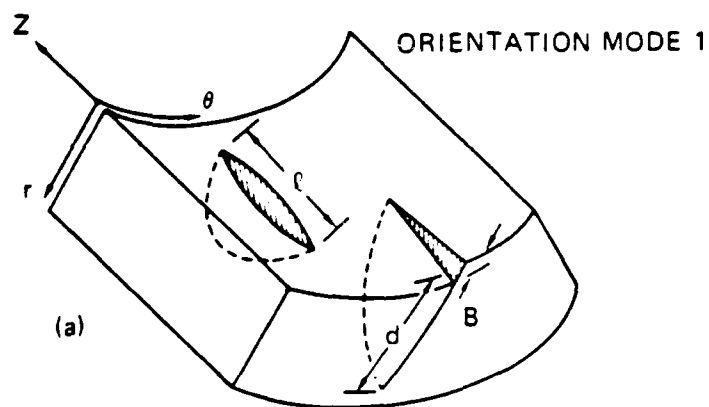
Nine RHA CFC experiments were performed during the second year of the program. The experimental configuration and explosive parameters for these experiments are shown in Figure 9 and in Table 2, along with the qualitative damage results.

Because quasi-static tensile tests, performed during the first year of the program, had revealed a significant anisotropy in tensile failure



MA-7893-170

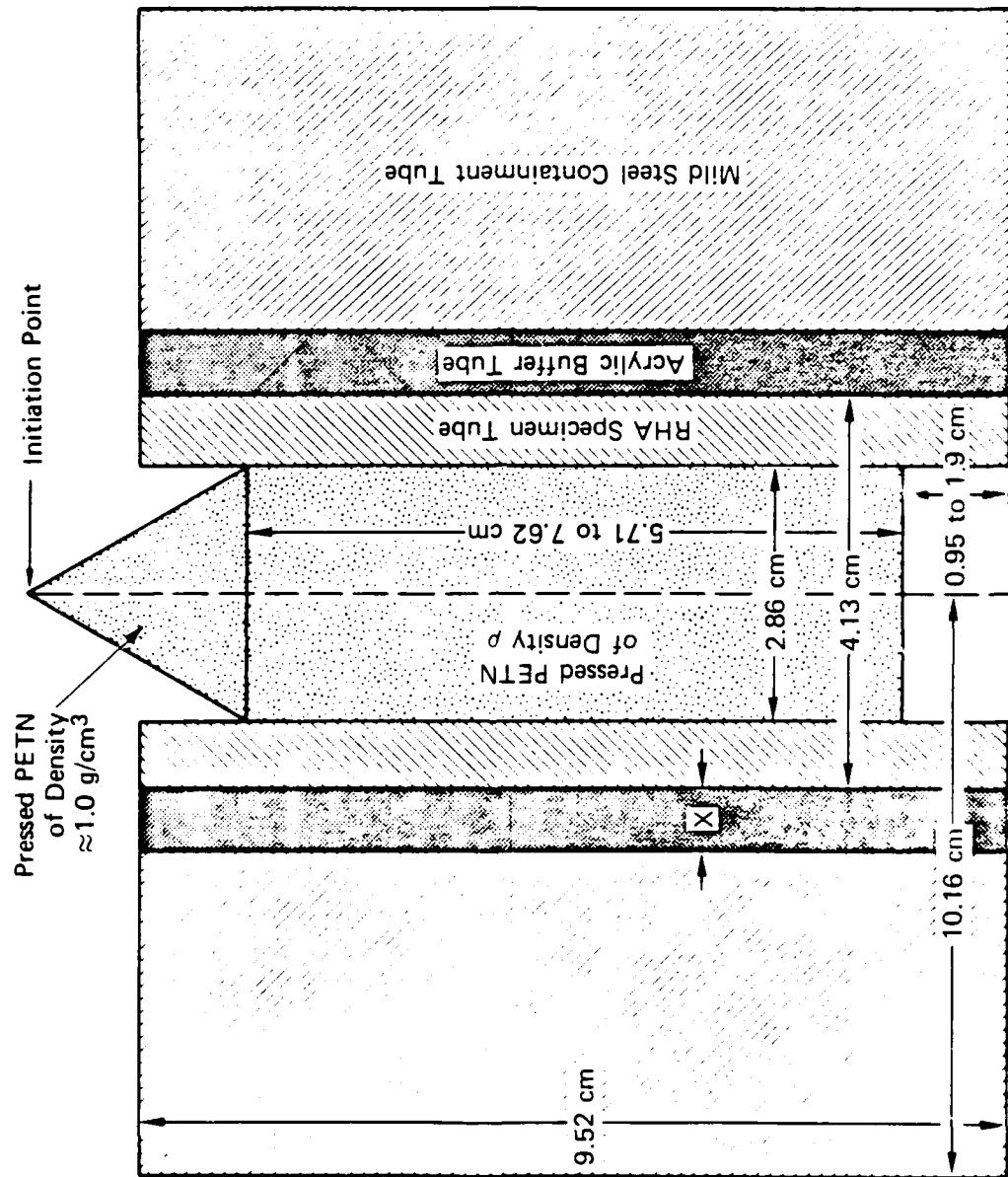
FIGURE 7 SCHEMATIC OF CFC EXPERIMENTS FOR STUDYING SHEAR BAND KINETICS



- l – Length in Direction Perpendicular to Slip Motion
- d – Depth Along 45° Slip Plane
- B – Shear Displacement Along Slip Plane
- Z – Axial Direction
- r – Radial Direction
- θ – Circumferential Direction

FIGURE 8 GEOMETRY AND NOMENCLATURE FOR SHEAR BANDS IN FRAGMENTING CYLINDER EXPERIMENTS

MA-5084-21B



X varies from 0.87 to 1.6 cm; ρ varies from 1.0 to ≈ 1.77 g/cm³

MA-7893-74

FIGURE 9 CROSS SECTION OF RHA CFC EXPERIMENTS

Table 2
PARAMETERS AND QUALITATIVE RESULTS FOR RHA CFC EXPERIMENTS

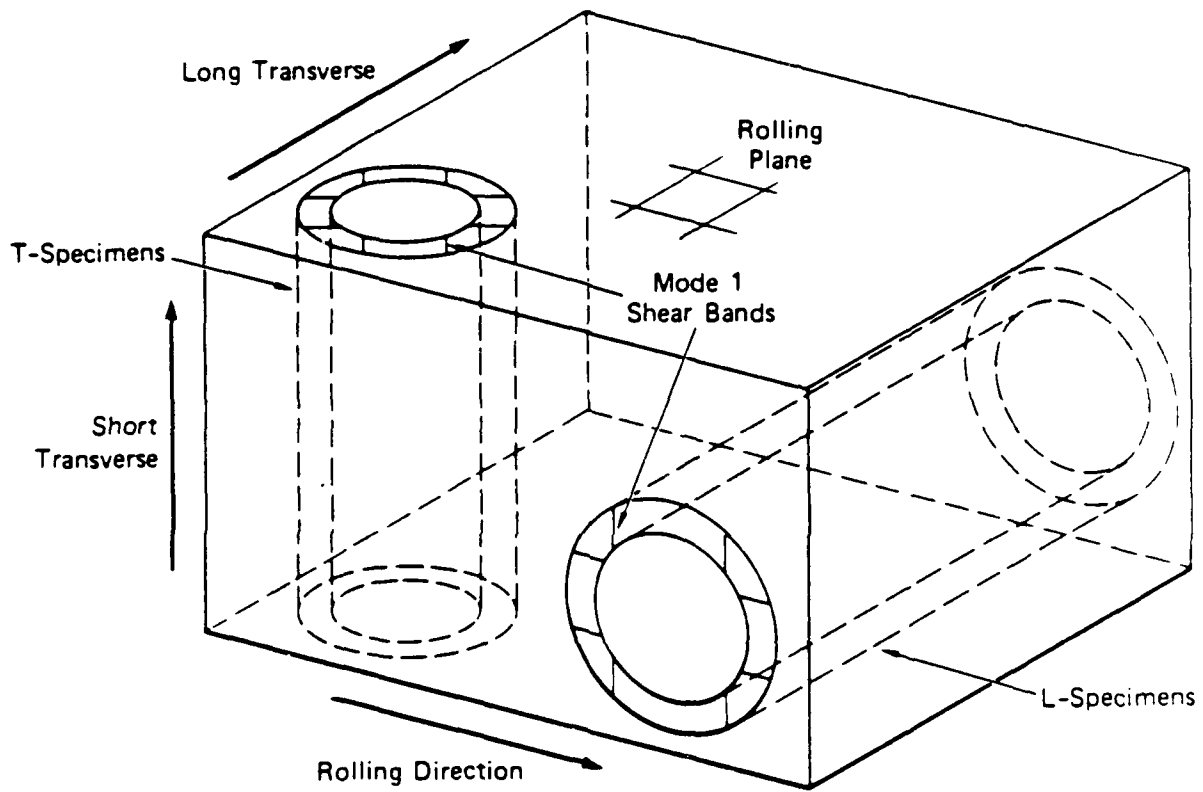
Specimen	Lucite Buffer Thickness (cm)	PETN Density (g/cm ³)	Calculated Detonation Pressure (kbar)	Qualitative Shear Banding Results
L-4*	0.873	1.2	122	Substantial Mode 1 banding concentrated in rolling direction
L-2	0.73	1.0	80	Same as L-4
T-1†	0.873	1.2	122	A few incipient Mode 1 bands (some tensile cracking on outer surface in midaxial region).
T-2	1.600	1.2	122	Few incipient Mode 1 bands. Moderate Mode 2 banding in midaxial region.
T-3	0.873	1.35	162	Incipient Mode 1 banding over most of inner surface (some tensile cracking as in T-1 above).
T-5	1.600	1.35	162	Extensive incipient Mode 1 banding. Few moderate Mode 2 bands in midaxial region.
T-7	1.600	1.47 to ≈ 1.77	202 to ≈ 324	Substantial Mode 1 banding. Substantial Mode 2 banding in narrow midaxial region.
T-9	1.27	1.54	228	Substantial Mode 1 banding. Mode 2 bands in midaxial region cuts specimen in two.
T-10	1.27	1.6	250	Same as T-9, with some fragmentation

*L-specimens have axes parallel to long transverse direction of RHA block.
†T-specimens have axes parallel to short transverse (through the thickness) direction.

properties in RHA,¹⁵ we expected a similar anisotropy to exist with respect to shear banding. Early experiments with RHA specimen tubes whose axes were in the long transverse direction of the RHA slab (the L-specimens, as shown in Figure 10) confirmed this expectation. The preponderance of shear bands in planes parallel to the rolling plane in specimens L-2 and L-4 (as seen in Figures 11 and 12), for example, clearly showed that shear banding will occur at lower strains in the rolling plane than in planes perpendicular to the rolling planes.

Once it became clear that by using L-specimens we could not obtain a uniform distribution of shear bands around the circumference of the specimen, we switched to T-specimens (whose axes were in the through-the-thickness direction) for which all the Mode 1 bands would lie in planes perpendicular to the rolling plane. The first four T-specimen experiments (T-1, T-2, T-3, and T-5), using PETN explosive densities similar to those in previous experiments,^{12,14} yielded only incipient Mode 1 shear banding. However, the final three experiments (T-7, T-9, and T-10), using much higher explosive densities, yielded significant quantities of both incipient and large shear bands, as well as some fragmentation. Photographs of these specimens are shown in Figures 13 and 14.

Shear band size distributions were obtained from the three RHA specimens that exhibited significant amounts of Mode 1 shear banding in planes perpendicular to the rolling plane. (No attempt was made to obtain quantitative damage estimates for the few Mode 2 bands found in these T-specimens, or for the Mode 1 bands in the L-specimens located in the rolling plane. These few bands localized in narrow regions would have yielded poor statistical results.) The cumulative size distributions in the various axial zones in shots T-7, T-9, and T-10 are shown in Figures 15, 16, and 17, respectively. The areal density of the shear bands intersecting the inner surface of the specimen tube and having a length (as defined in Figure 8) greater than L , is plotted against L . As expected, for each shot the zones at or near the ends of the specimen exhibited lower shear band densities than those in the middle.



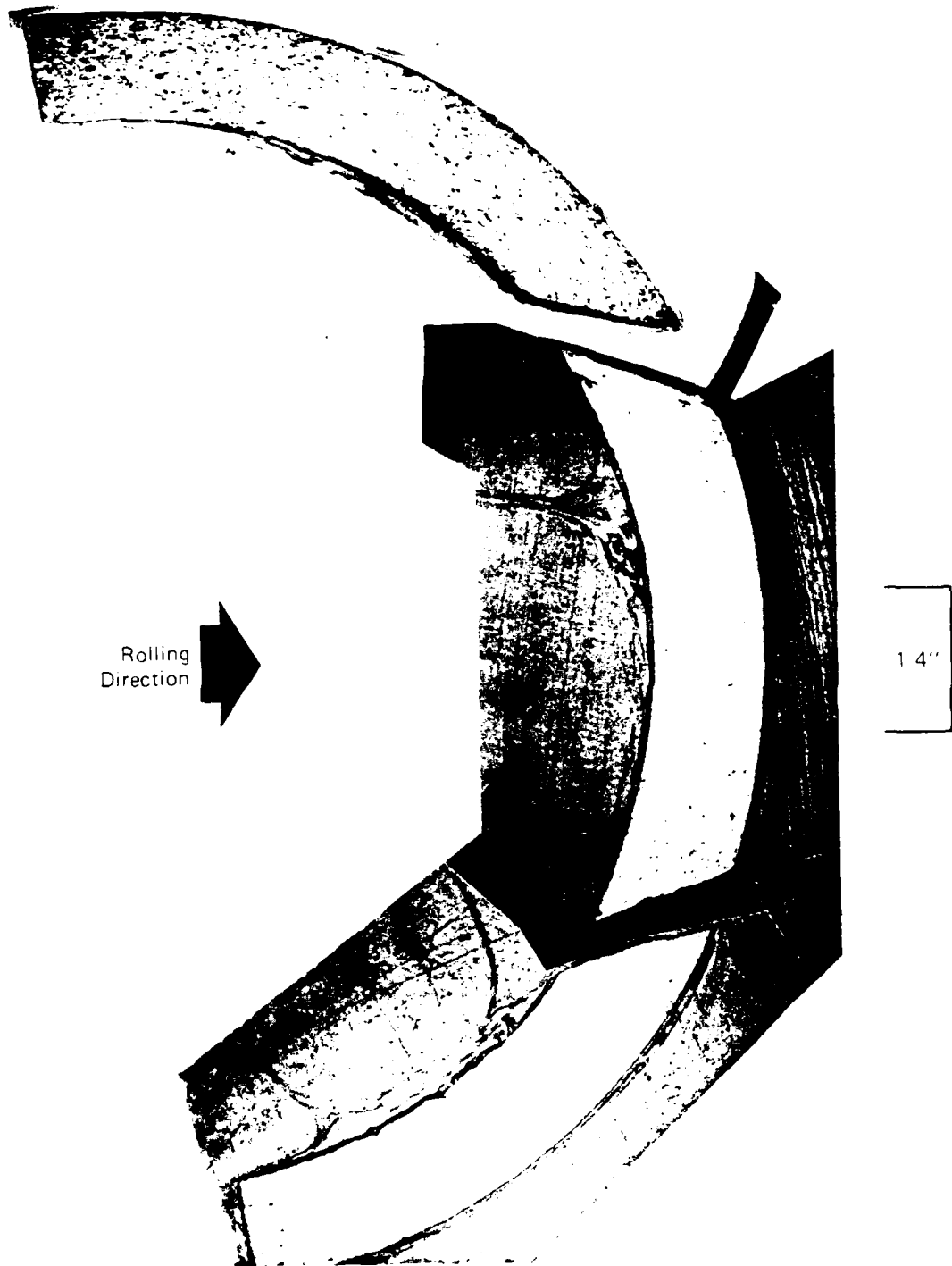
MA-7893-47A

FIGURE 10 CFC SPECIMENS MACHINED FROM RHA SLAB, SHOWING MODE 1 SHEAR BANDS IN PLANES PERPENDICULAR TO ROLLING PLANE



MP 7893.43

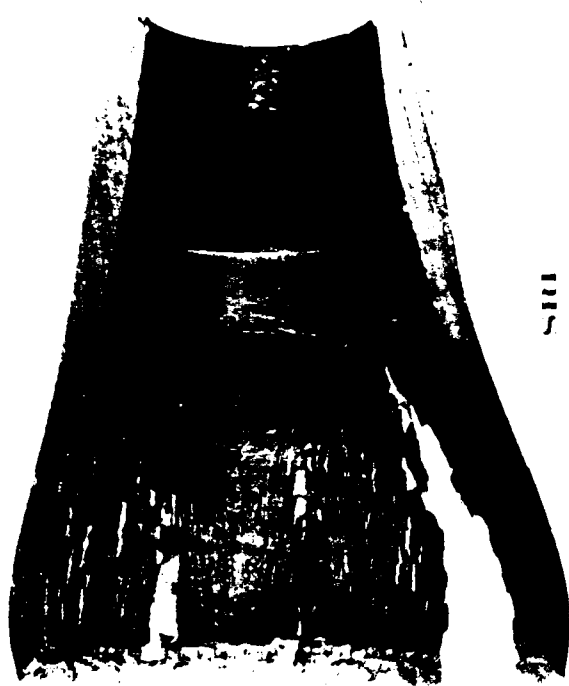
FIGURE 11 TWO VIEWS OF HALF OF THE RHA SPECIMEN TUBE L-4 RECOVERED FROM CFC EXPERIMENT



MP 7893 44

FIGURE 12 POLISHED AND ETCHED SECTION THROUGH RHA SPECIMEN TUBE L-4
SHOWING PREPONDERANCE OF SHEAR BANDING DAMAGE IN ROLLING
DIRECTION

(Plane is cut at a distance of 2-3/8" from bottom of specimen tube.)



(a)



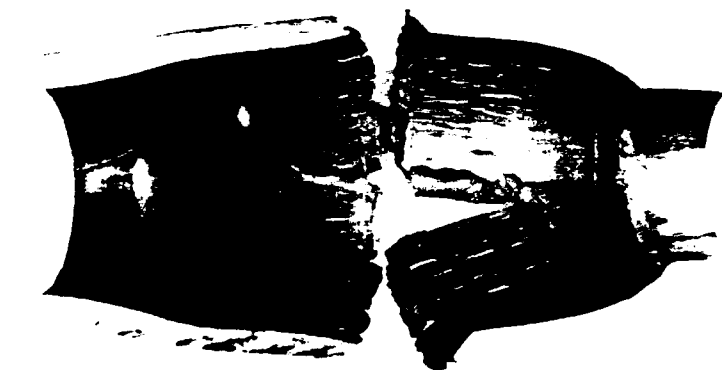
(b)

MA-7893-75

FIGURE 13 TWO VIEWS OF HALF OF THE RHA SPECIMEN TUBE T-7 RECOVERED FROM CFC EXPERIMENT
Detonation proceeds from top to bottom.



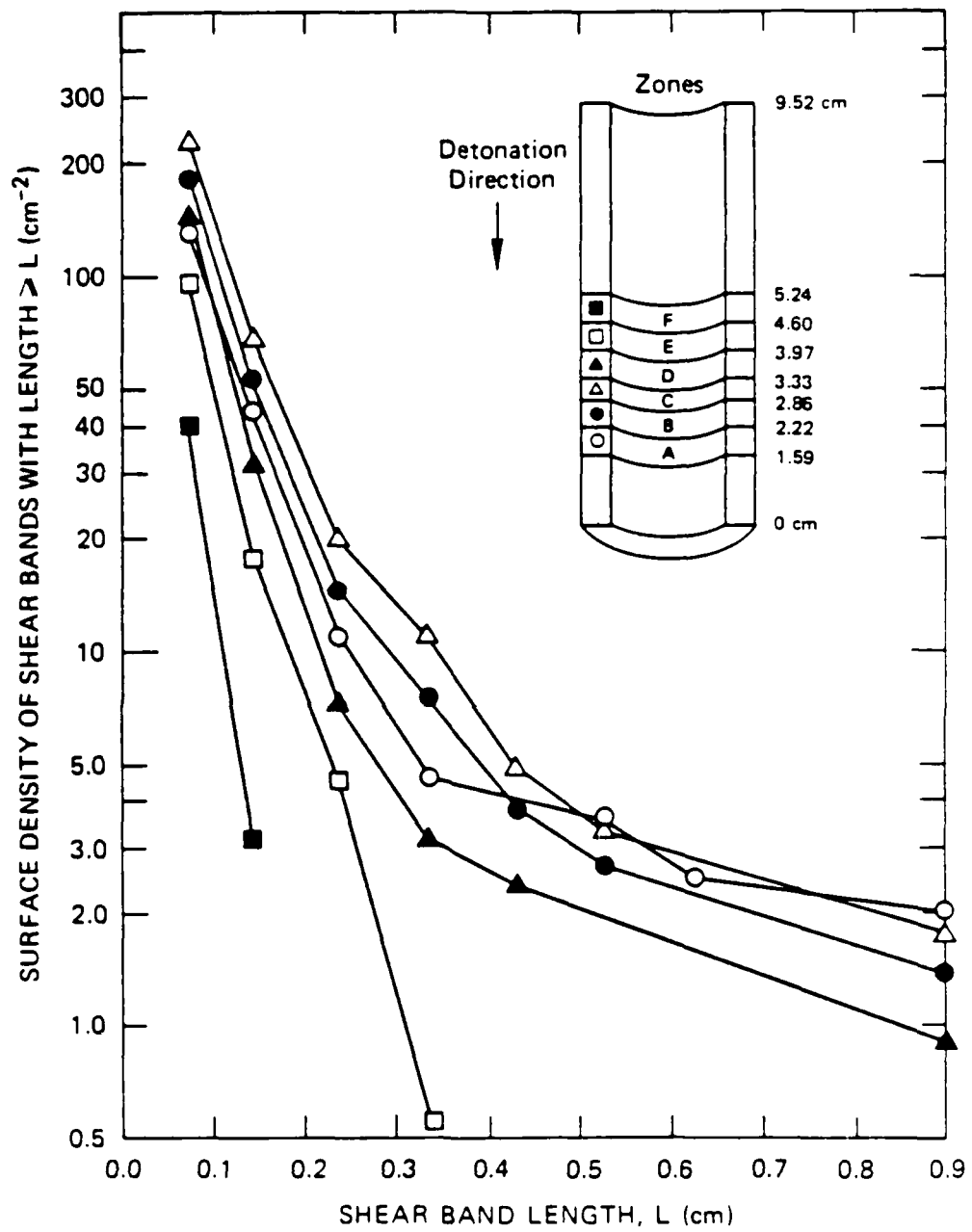
(a)



(b)

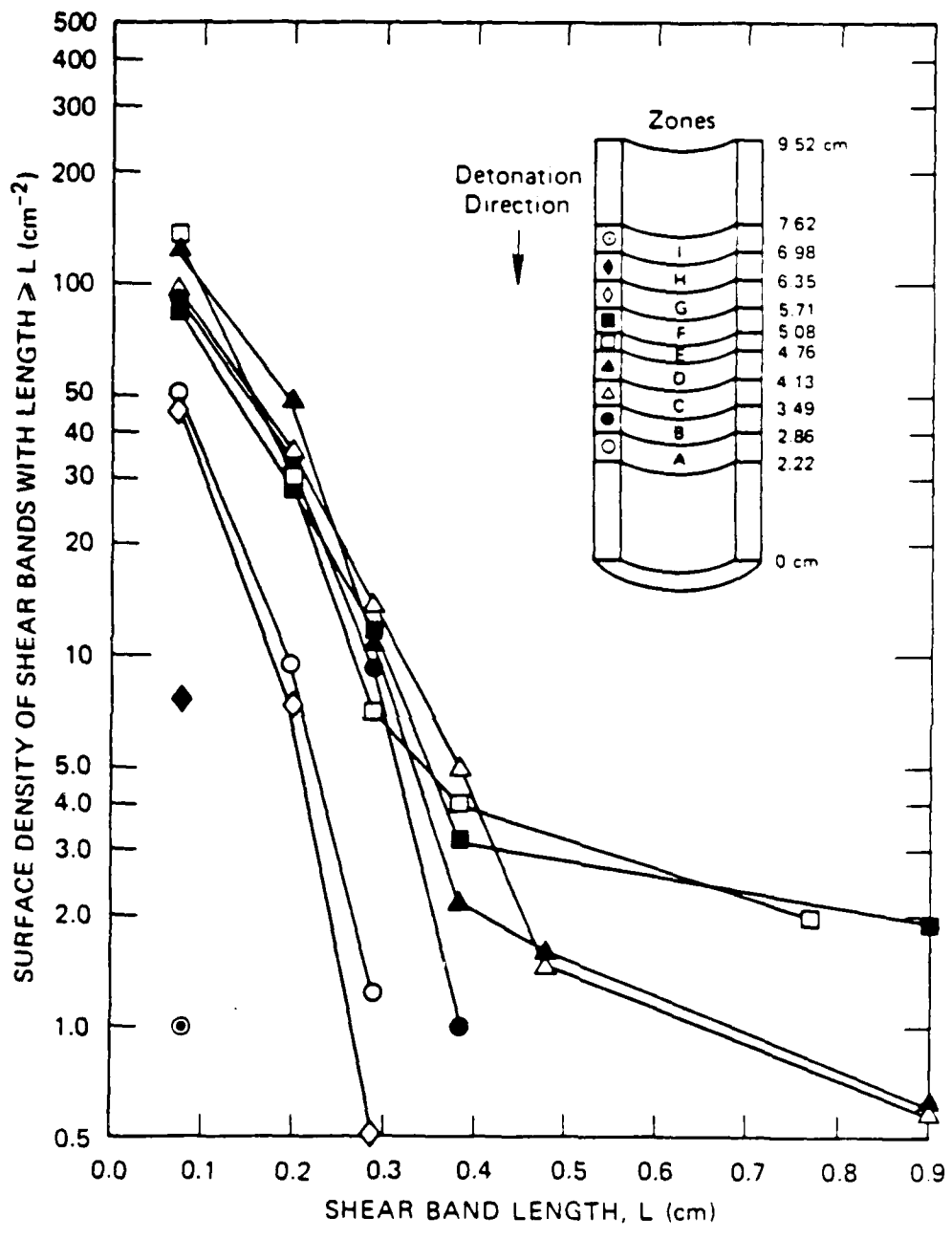
MP 7833 76

FIGURE 14 HALF OF RHA SPECIMEN (a) T 9, AND (b) T 10 RECOVERED FROM CFC EXPERIMENTS
Detonation proceeds from top to bottom.



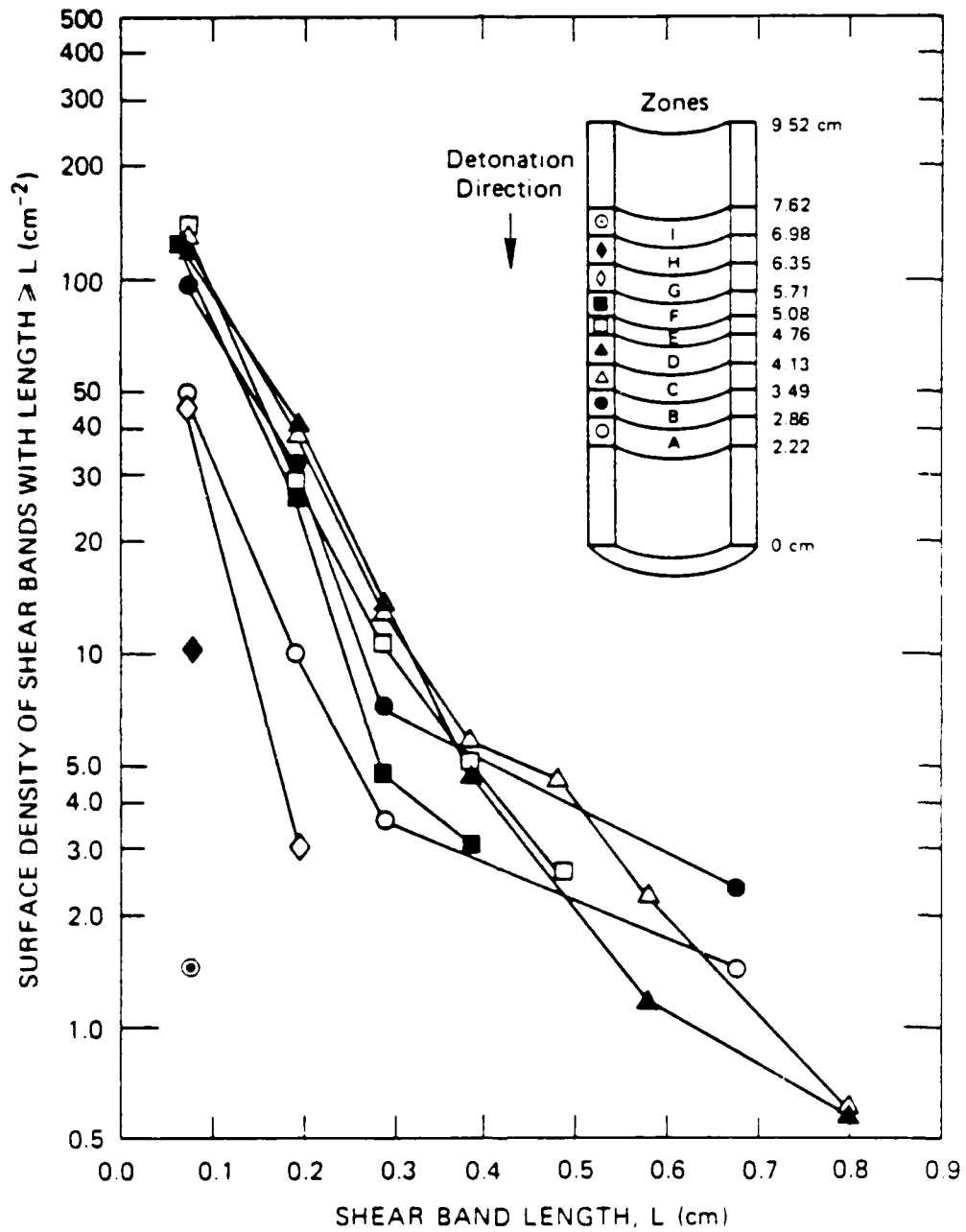
MA-7893-151

FIGURE 15 CUMULATIVE SIZE DISTRIBUTIONS OF SHEAR BANDS FROM RHA SHOT T-7



MA-7893-152

FIGURE 16 CUMULATIVE SIZE DISTRIBUTIONS OF SHEAR BANDS FROM RHA SHOT T-9



MA-7893-153

FIGURE 17 CUMULATIVE SIZE DISTRIBUTIONS OF SHEAR BANDS FROM RHA SHOT T-10

There is a significant uncertainty in the plotted values for the shear band density for lengths greater than about 0.7 cm because the small number of these large bands produce poor statistics. There is also a significant uncertainty in the plotted values for lengths less than 0.1 cm, because it was difficult to see and accurately count the large number of small bands (this was particularly true of RHA because the low carbon content minimizes the martensitic transformations that appear as white etching bands). So the distributions are most accurate in the intermediate length range.

CFC Experiments with DU

A series of three CFC experiments were performed using DU. The experimental configuration and explosive parameters for these experiments are shown in Figure 18 and Table 3, along with the qualitative damage results. Note that the buffer thickness was kept constant for all three shots, but the PETN density and hence the detonation pressure was varied.

Predictions from Critical Strain Theory

We expected that DU would exhibit shear bands at lower plastic strains than those in the other materials (RHA or 4340 steel, $R_c 40$) with which we have performed CFC studies. This expectation was based on calculations using our previously derived formula¹⁵ for critical strains for shear band initiation:

$$\bar{\epsilon}_{cr}^p = \left(\frac{2\rho E_m n(n+1)}{\alpha\tau_0(2n+1)} \right)^{\frac{1}{n+1}} \quad (1)$$

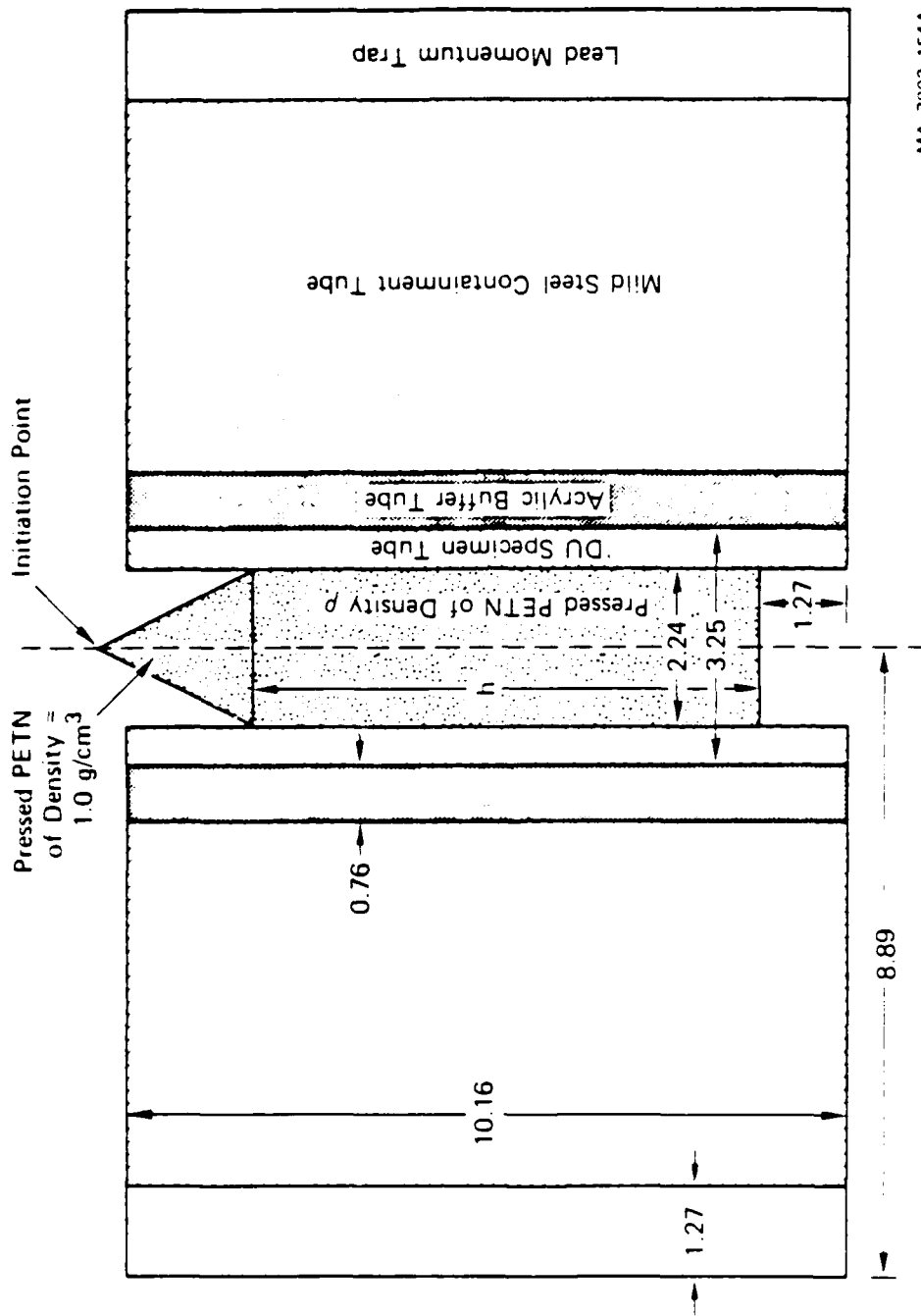
where

$\bar{\epsilon}_{cr}^p$ \equiv equivalent plast strain at which shear bands may nucleate

ρ \equiv density

E_m \equiv specific internal energy at incipient melt.

τ_0 and n are defined by the strain-hardening formula



MA-7893-154A

FIGURE 18 CROSS SECTION OF DU CFC EXPERIMENTAL APPARATUS

All dimensions in cm. ρ varies from 0.8 to 1.2 g/cm³, h varies from 5.87 to 7.62 cm.

Table 3

PARAMETERS AND QUALITATIVE RESULTS FOR DU CFC EXPERIMENTS

Shot	PETN Density ρ (g/cm ³)	Explosive Column Height, h (cm)	Acrylic Buffer Thickness (cm)	Expected Peak Detonation Pressure (kbar)	Qualitative Damage Results
10	1.20	7.62	0.762	120	Complete fragmenta- tion by Mode I shear banding
11	0.95	7.62	0.762	74	Substantial Mode I shear banding, moderate fragmenta- tion.
12	0.80	6.67	0.762	45	Substantial Mode I shear banding, minor fragmentation

$$\tau = \tau_0 (\bar{\epsilon}^p)^\alpha$$

where

τ \equiv shear stress

$\bar{\epsilon}^p$ \equiv equivalent plastic strain

and α is defined by the thermal softening function

$$F\left(\frac{W}{E_m}\right) = \left(1 - \frac{\alpha W}{E_m}\right)^{1/2}$$

where

W \equiv specific energy of the plastic deformation.

Table 4 gives the calculated critical strains for various materials, including DU, along with the material parameters, as defined above, that were used in the calculation. The critical strain calculated for DU is 0.10, as compared with 0.56 for RHA and 0.19 for 4340 steel, $R_c 40$. Previous CFC experiments on RHA and 4340 steel have shown this formula, which was derived from plastic instability theory, to be useful in predicting approximate strains for shear band initiation.

Qualitative Experimental Results

Examinations of the recovered specimens showed that our predictions were reasonable. Figure 19 shows photographs of the two tubes that did not completely fragment (shots 11 and 12), sliced in half axially to allow easier inspection. Although the shear bands on the inner surface are somewhat obscured by the substantial oxidation or scale, it appears that for shot 12, Mode I shear bands appear at radial expansions of about 10%.

As seen in Figure 19(a), a transverse cut near the midaxial plane was made in one DU piece recovered from shot 11. The ground and electro-polished surface (in Figure 20) shows several large cracks and several smaller bands crossing the specimen at approximately 45° to the radial direction. Metallographic examination showed that both the cracks and

Table 4

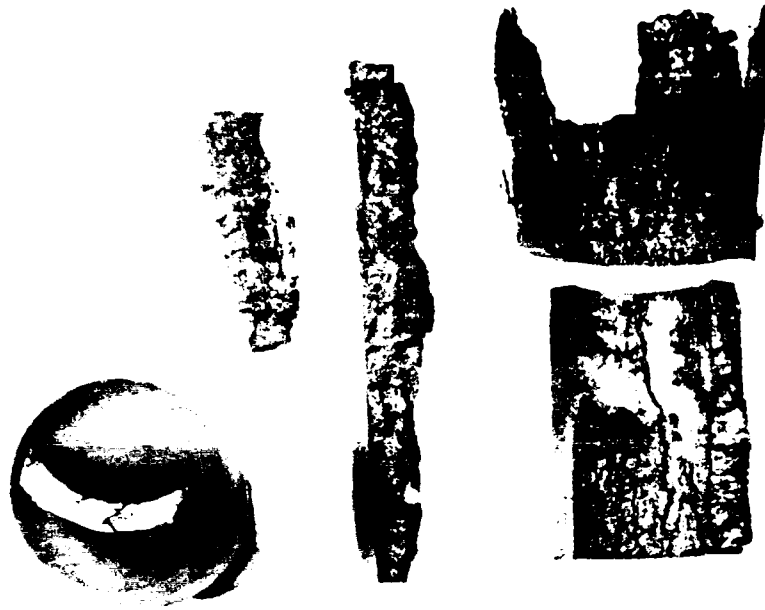
CRITICAL STRAINS FOR SHEAR BAND INITIATION
IN VARIOUS MATERIALS, AS CALCULATED FROM EQUATION (1),
AND MATERIAL PARAMETERS USED IN THE CALCULATIONS

Material	$\bar{\epsilon}_{cr}^p$	τ_0 (dyne/cm ²)	n	α	(ergs/g)
4340 Steel, R _c 40	0.19	2.70 x 10 ¹⁰ (22)	0.15(22)	3.23(22)	6.14 x 10 ⁹ (23)
4340 Steel, R _c 35	0.28	2.50 x 10 ¹⁰ (22)	0.15(22)	2.25(22)	6.14 x 10 ⁹ (23)
RHA, R _c 22	0.56	1.38 x 10 ¹⁰ (16)	0.19(16)	2.25*	6.14 x 10 ⁹ *
Hadfield steel	1.09	2.28 x 10 ¹⁰ (24)	0.59(24)	1.59(24)	6.14 x 10 ⁹ (23)
Low carbon steel	1.15	1.08 x 10 ¹⁰ (25)	0.28(25)	1.70(26)	6.14 x 10 ⁹ (23)
Ti-6Al-4V	0.09	1.37 x 10 ¹⁰ (27)	0.068(27)	2.86(26)	5.18 x 10 ⁹ (23)
DU-3/4Ti	0.10	2.35 x 10 ¹⁰ †	0.22†	2.22(28)	7.36 x 10 ⁸ (26)

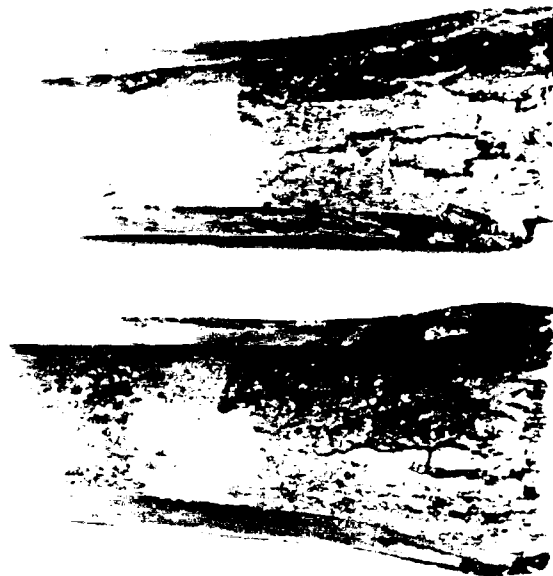
Note: Numbers in parentheses refer to the sources for the data, which are listed in the references.

*Best estimates from available data on similar materials.

†Data obtained in this program—see Section II.



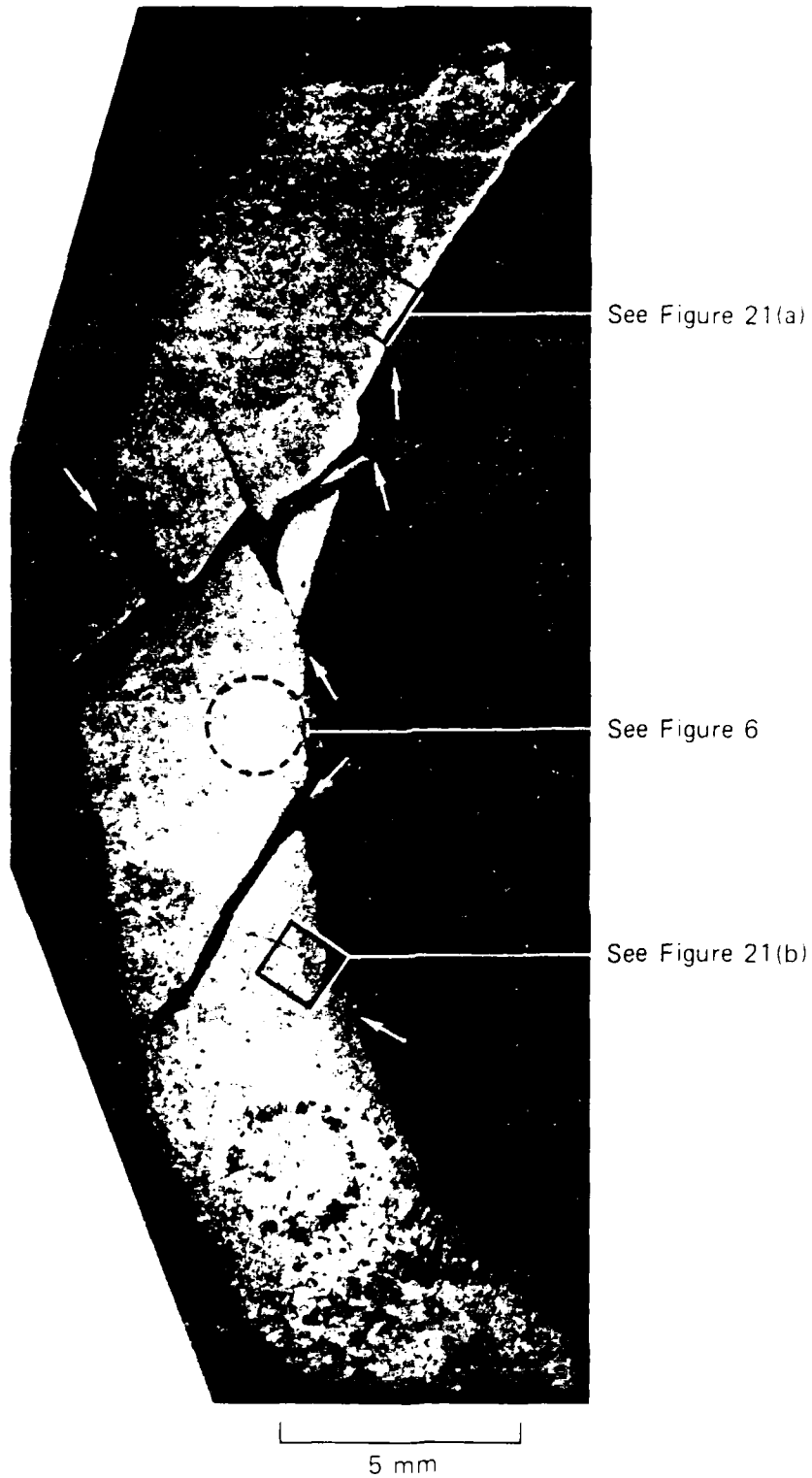
(a) SHOT 11



(b) SHOT 12

MP-7893-155

FIGURE 19 SLICED DU TUBES RECOVERED FROM CFC EXPERIMENTS



See Figure 21(a)

See Figure 6

See Figure 21(b)

5 mm

MP-7293-156A

FIGURE 20 TRANSVERSE SLICE NEAR MIDAXIAL PLANE OF A PORTION OF DU SPECIMEN RECOVERED FROM CFC SHOT 11

Arrows point to shear bands confirmed by metallographic examination.

the bands are associated with the adiabatic shearing process. Higher magnification views of two of the shear bands (Figure 21) reveals a white, featureless zone bounded by a heavily sheared microstructure, as evidenced by the curvature of the martensite platelets adjacent to the band. This structure is similar to that observed previously in a DU penetrator fragment.¹⁶

Anisotropy

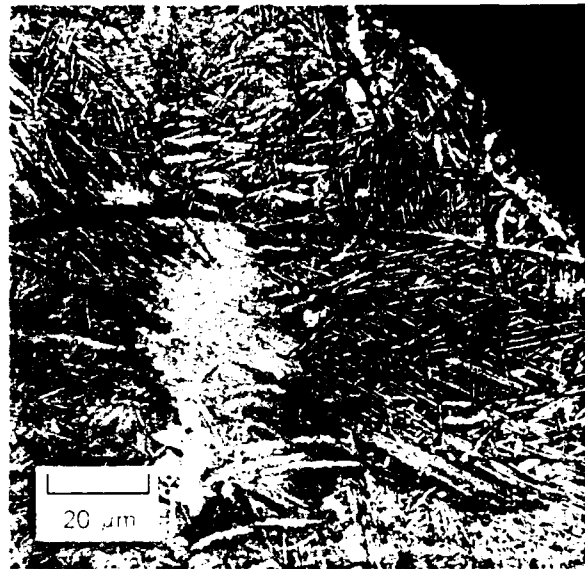
The CFC experiments are designed to produce large quantities of Mode 1 bands because the Mode 1 bands lie in planes of maximum shear strain (parallel to the cylinder axis and at 45° from the radial and circumferential directions). The DU CFC specimens were machined from extruded rod in the only orientation feasible, that is, with the specimen axis co-axial with the rod. The Mode 1 shear band orientation produced in the CFC experiments is, unfortunately, not the same orientation as bands primarily responsible for penetrator erosion during armor penetration. Previous phenomenological studies with several different penetrator materials^{12,13,15} have shown that such erosion is caused by Mode 2 bands: bands parallel to the circumferential direction and at 45° from the axial and radial directions.

There may be a few Mode 2 bands in the recovered DU specimens. For example, the shear lip at the extreme right edge of Figure 13(b) is a Mode 2 band caused by edge effects. However, our experience indicates that in a CFC experiment only Mode 1 bands are produced in large enough numbers and over a wide enough region to yield quantifiable results. Therefore, we will have to use the results of the Mode 1 analysis to predict Mode 2 damage. This might cause difficulties in the case of significant shear banding anisotropy.

We have two significant, although not totally conclusive, pieces of evidence indicating that anisotropy is not a major factor in this DU alloy. First, there was negligible Mode 2 shear banding observed in the recovered CFC specimens. This suggests that planes in the Mode 2 orientation in DU are not much weaker in their resistance to shear banding



(a)



(b)

MP-7893-157

FIGURE 21 TWO SHEAR BANDS IN DU (Enlarged from Figure 20)
Note curvature of martensite platelets adjacent to shear bands.

than those in the Mode 1 orientation. In contrast, RHA, which was found to exhibit just such a shear banding anisotropy, did show significant Mode 2 shear banding in recovered CFC specimens whose axes were oriented transverse to the rolling plane (see Figure 14, for example).

Second, static tensile tests performed on DU (as reported in the Section II) showed only a negligible anisotropy between the axial and transverse directions for failure strain. We believe the absence of anisotropy in tensile failure is a good predictor of its absence in shear failure, since anisotropy in both failure modes is thought to arise from the same microstructural features.

Quantitative Damage Analysis

Of the three DU CFC experiments performed, only one--shot 12 [as shown in Figure 9(b)]--appeared to have achieved a sufficiently low level of shear banding to allow for a quantitative damage assessment. However, the inside surfaces of the recovered tube was covered by a thick black coating, undoubtedly the result of the reaction between the pyrophoric uranium and the explosive products. Because the thick coating obscured much of the detail of the shear banding damage, it was necessary to remove the coating before proceeding with the analysis.

After several different chemical cleaning techniques (based on established procedures for removing uranium oxide) proved unsatisfactory, we tried an electrochemical technique recommended by personnel at the Lawrence Livermore Laboratory. This technique used a solution of 50 mL of perchloric acid, 200 mL of acetic acid, and 2 grams of citric acid, cooled by a liquid nitrogen bath. A current density of 100 to 150 mA/cm² was applied to the specimen for a few minutes, using a stainless steel cathode immersed in the solution to complete the circuit. The electrochemical technique removed all the scale except for a thick band that was subsequently shown to be a carbon-based material, rather than uranium oxide. Fortunately this band was easily removed by brushing and scraping the surface.

The cleaned specimen is shown in Figure 22, along with the axial zones used in the quantitative shear band damage analysis. The number of shear bands of various lengths were counted for each zone, and the resultant cumulative size distributions are shown in Figure 23. Note that the uncertainty in these surface density curves is greater than that for RHA or 4340 steel. The condition of the DU surface, even after cleaning, tended to obscure bands less than a couple of mm in length and to make it difficult to determine if a long band is one band, or two or more joined together.

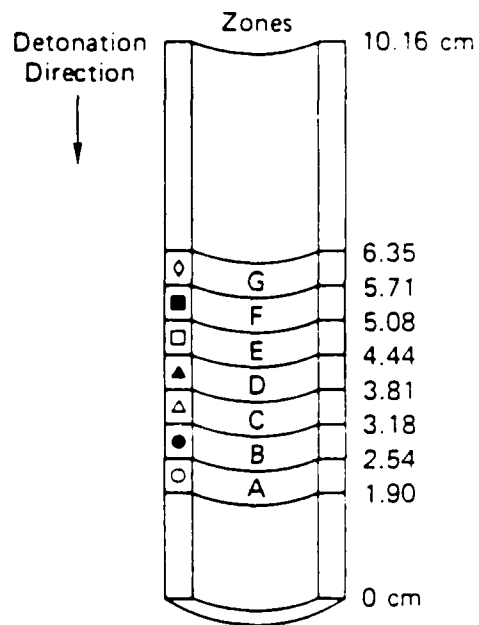
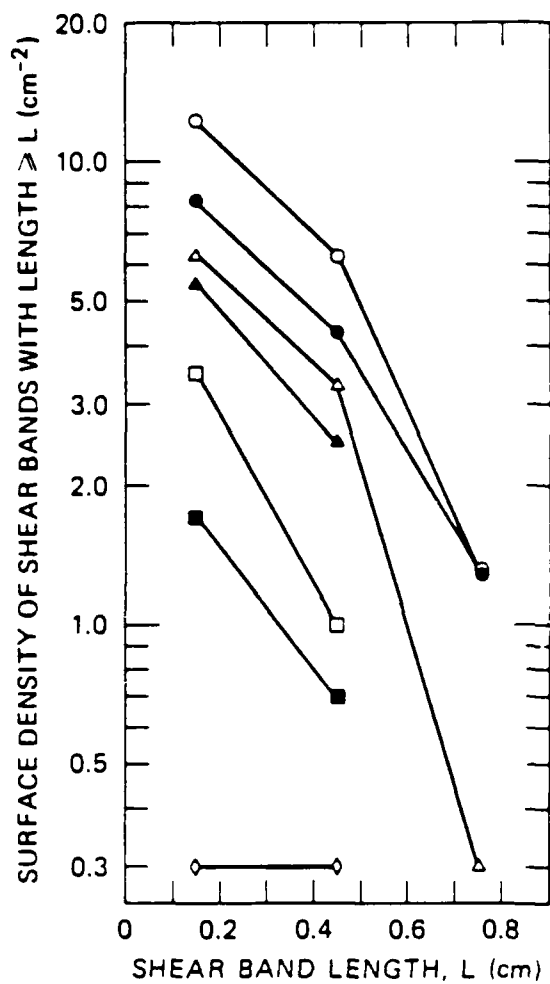
The quantitative shear band results, along with the measurements of final wall thickness and diameter as a function of axial position, are therefore now available for current and future comparison with computer simulations to determine the shear band kinetics parameters of DU.



IP 3291-150

FIGURE 22 INSIDE SURFACE OF SHEAR BAND DAMAGED END OF HALF OF DU TUBE
RECOVERED FROM CFC SHOT 12

Labeled axial zones 6.35 mm wide are used in quantitative analysis.



MA-7893-162A

FIGURE 23 CUMULATIVE SIZE DISTRIBUTIONS OF SHEAR BANDS FROM DU SHOT 12

IV DETERMINATION OF SHEAR BAND KINETICS PARAMETERS FROM CFC EXPERIMENTS

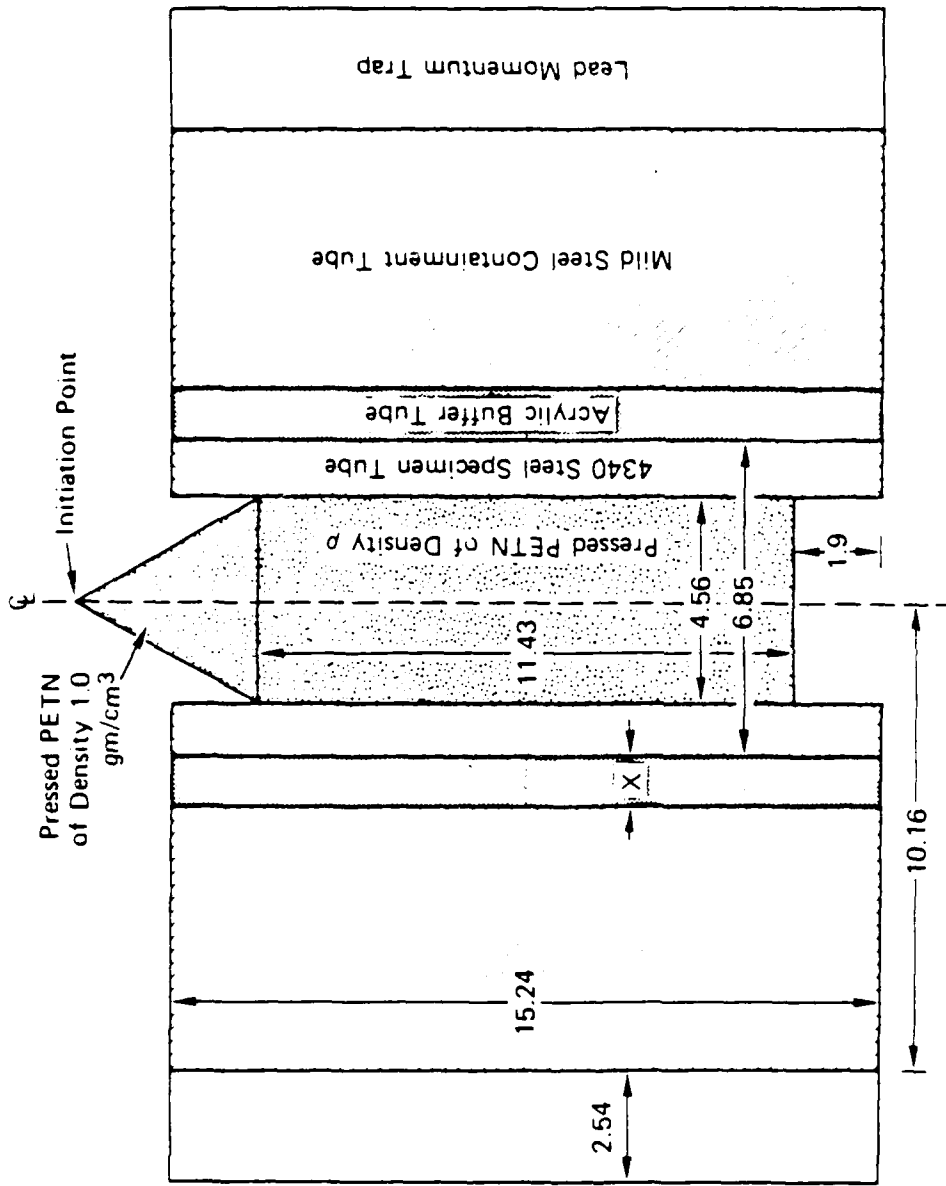
The method for determining the shear band kinetics parameters from CFC experiments is discussed in this section. This method, which involves fitting the revised SHEAR3 model (which is fully derived and described in Volume II of this report) to CFC data, will be illustrated here for both RHA and 4340 steel ($R_c 40$) material.* First, the general procedure is outlined, and the experimental data are examined. Then guidelines for matching the model to the data are discussed, and the resulting parameters are presented.

CFC Data

To determine the shear band kinetics parameters for both RHA and 4340 steel, we used data from previously performed CFC experiments spanning a wide range of damage from incipient shear banding to substantial fragmentation. These include, for RHA, CFC tests T-2, T-9, and T-10, described in Section III (see Figure 9 and Table 2); and for 4340 steel, CFC tests 2 and 8,¹⁴ whose geometry and explosive parameters are shown in Figure 24.

The primary data obtained from the CFC tests are the final shape of the recovered specimen tubes and the shear band size distributions. Preliminary C-HEMP simulations are first performed for each experiment, with the SHEAR3 model representing the test material but with no shear banding allowed. For the low-damage experiments (RHA test T-2 and 4340 steel test 2), the computed final shape of the tube is compared with

*Although shear band kinetics parameters had been previously obtained¹³ for 4340 steel ($R_c 40$) for an earlier version of SHEAR3, it was felt that the changes made in the revised SHEAR3, particularly in the nucleation algorithm, warranted a redetermination of these parameters.



Test	X (cm)	ρ (g/cm ³)	Calculated Detonation Pressure (kbar)
2	1.27	1.20	122
8	0.95	1.47	204

MA 6408-3A

FIGURE 24 CROSS SECTION OF 4340 STEEL (R₄₀) CFC EXPERIMENTS
All dimensions in cm except where otherwise noted

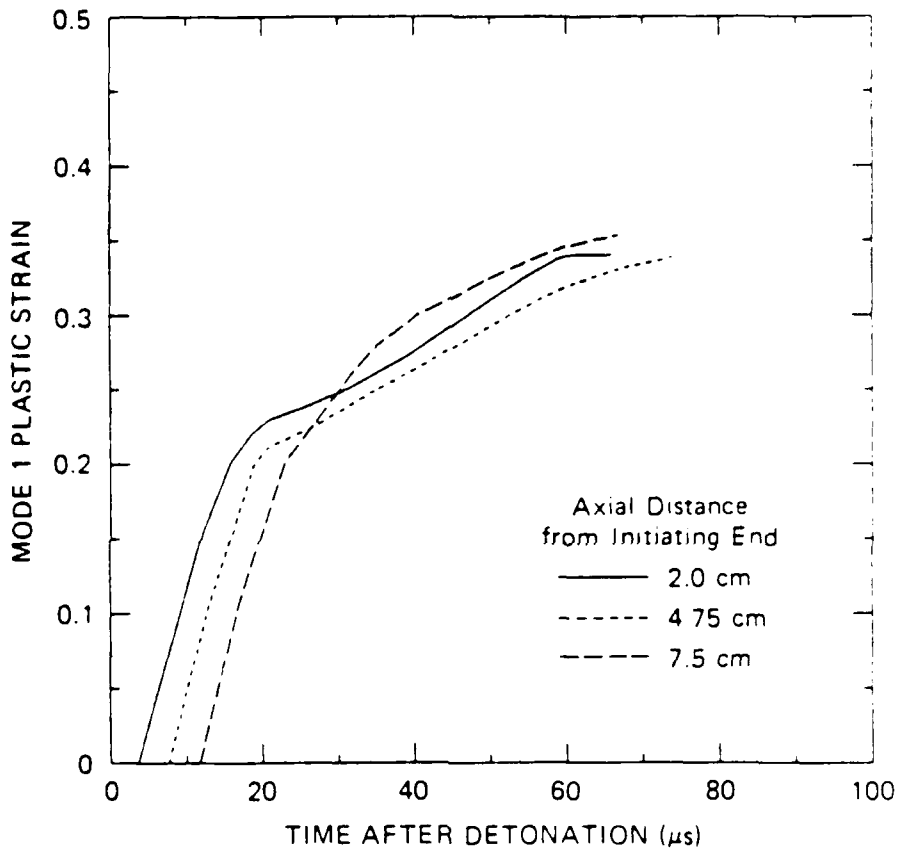
that obtained experimentally to verify that the calculation simulates the detonation and the homogeneous deformations of the specimen tube with acceptable accuracy* (such a comparison is not useful for the higher-damage experiments, since the damage can significantly affect the final shape).

From the preliminary simulations we obtained histories of the strains in each damage mode, as well as the equivalent plastic strain and the various stresses. Plots of the Mode I strain histories (as defined in Figure 8) are shown in Figures 25 to 29 for five CFC tests considered here. The three histories shown for each test were obtained for cells in the midthickness position radially and at axial positions approximately one-fourth, one-half, and three-fourths of the length of the tube, respectively, from the initiating end.

Plastic strain rate histories were also obtained; a sample is shown in Figure 30 for RHA test T-9. The strain rate shows an initial pulse of 15- to 20- μ s duration corresponding to the passage of the detonation wave in the explosive. The second pulse of significantly lower peak strain rate but longer pulse duration is caused by the rarefaction wave that is reflected from the radial free surface of the containment vessel. The plot in Figure 31 of the strain rate versus strain also shows this two-pulse structure. The threshold strain for nucleating shear bands is usually reached after the end of the first pulse; therefore, the lower strain rates in the second pulse govern the nucleation and growth processes.

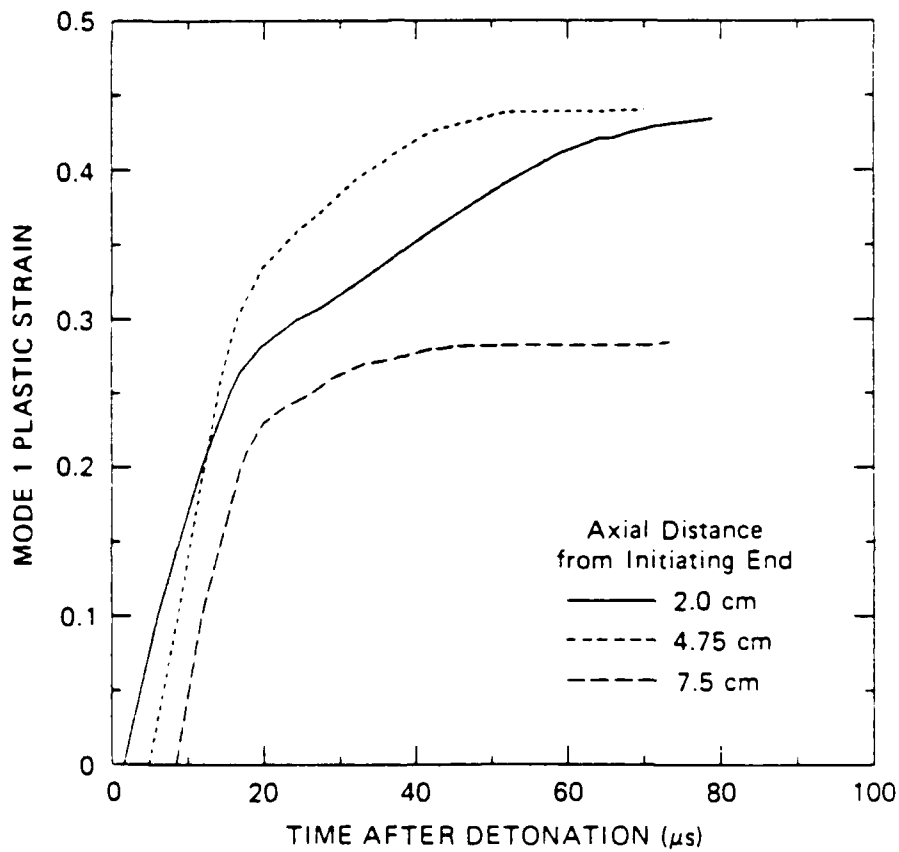
Measured shear band size distributions for RHA tests T-9 and T-10 have been shown previously in Figures 16 and 17, respectively (those for 4340 steel tests 2 and 8 are reported in reference 14). The distributions for zones corresponding to the axial positions for which the strain histories shown above were obtained were fitted to the following exponential form:

*An accurate comparison of shapes is a necessary but not sufficient proof that the experiment is well-represented by the simulation.



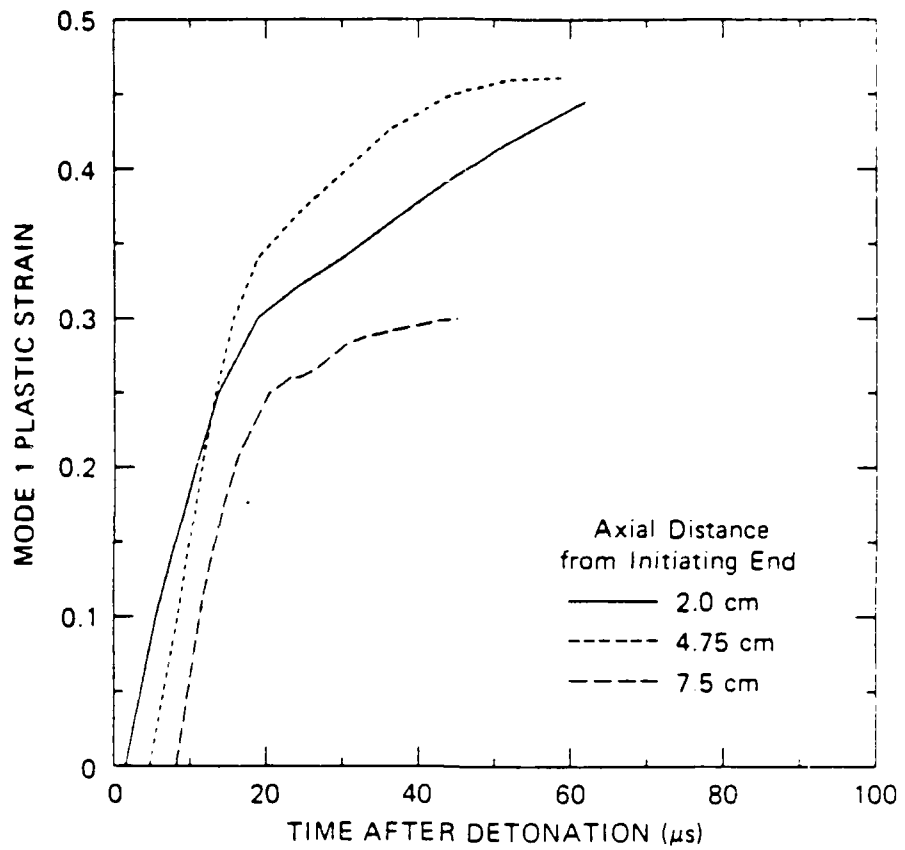
MA-7893-200

FIGURE 25 CALCULATED PLASTIC STRAIN HISTORIES FOR RHA TEST T-2



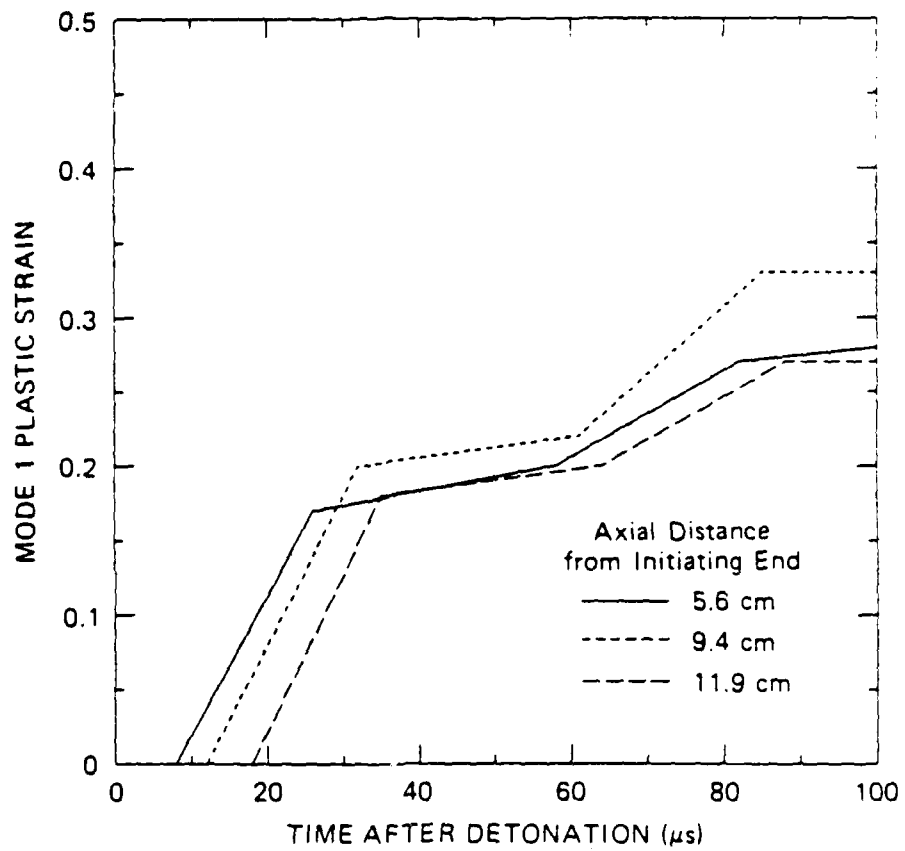
MA-7893-201

FIGURE 26 CALCULATED PLASTIC STRAIN HISTORIES FOR RHA TEST T-9



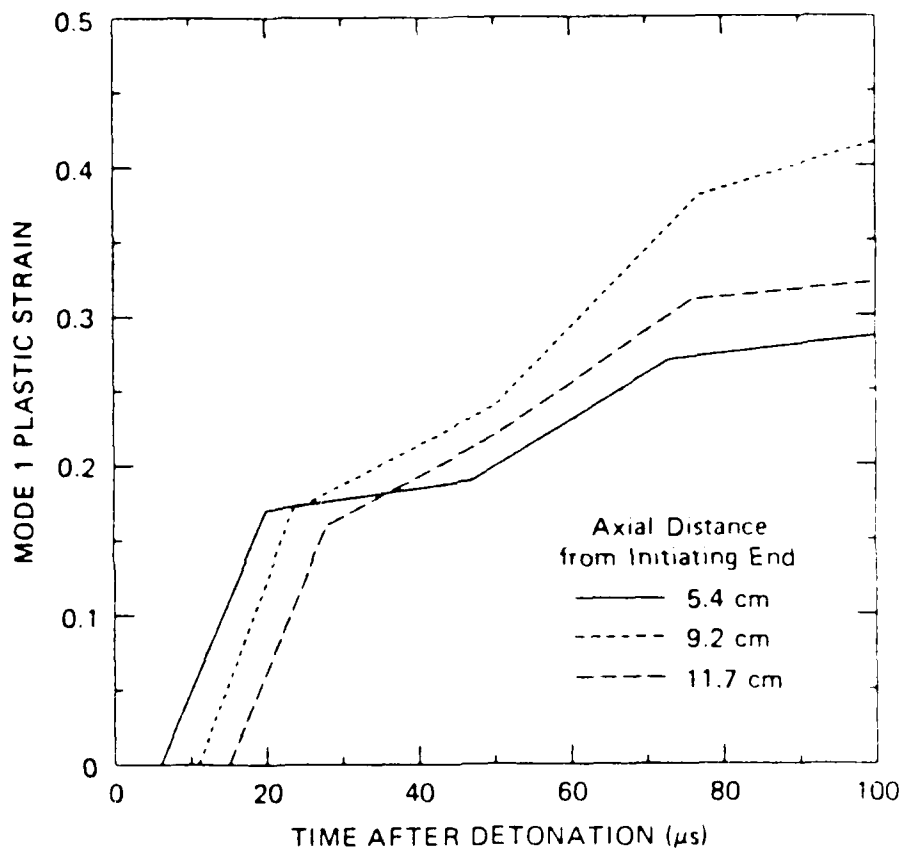
MA-7893-202

FIGURE 27 CALCULATED PLASTIC STRAIN HISTORIES FOR RHA TEST T-10



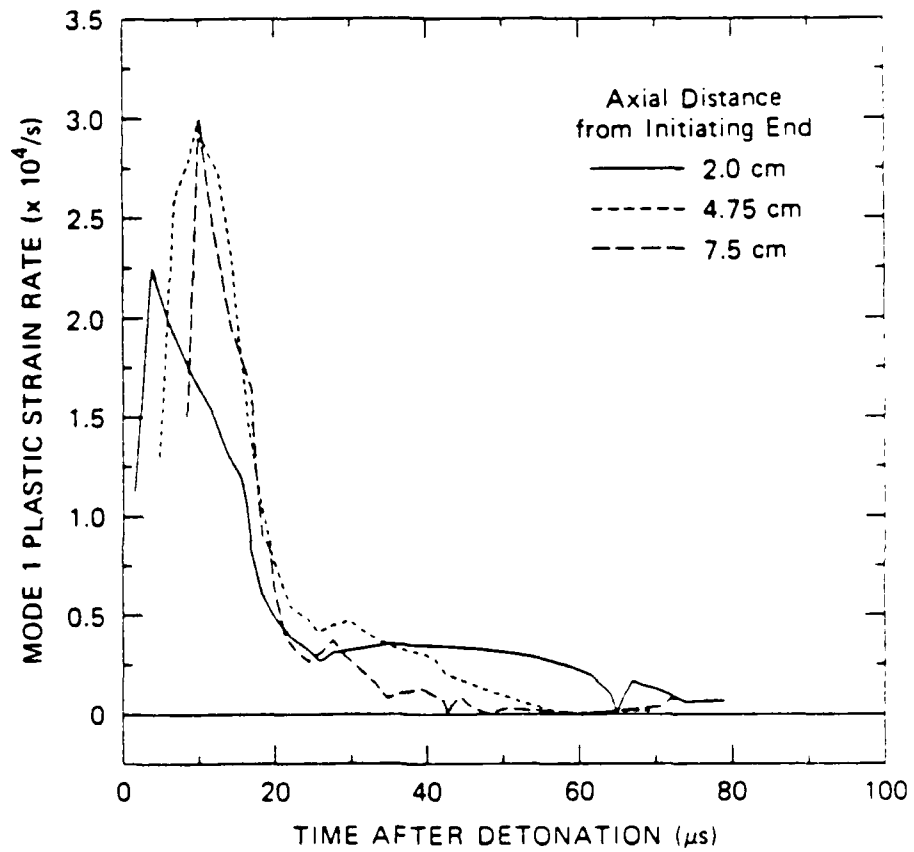
MA-7893-198

FIGURE 28 CALCULATED PLASTIC STRAIN HISTORIES FOR 4340 STEEL TEST 2



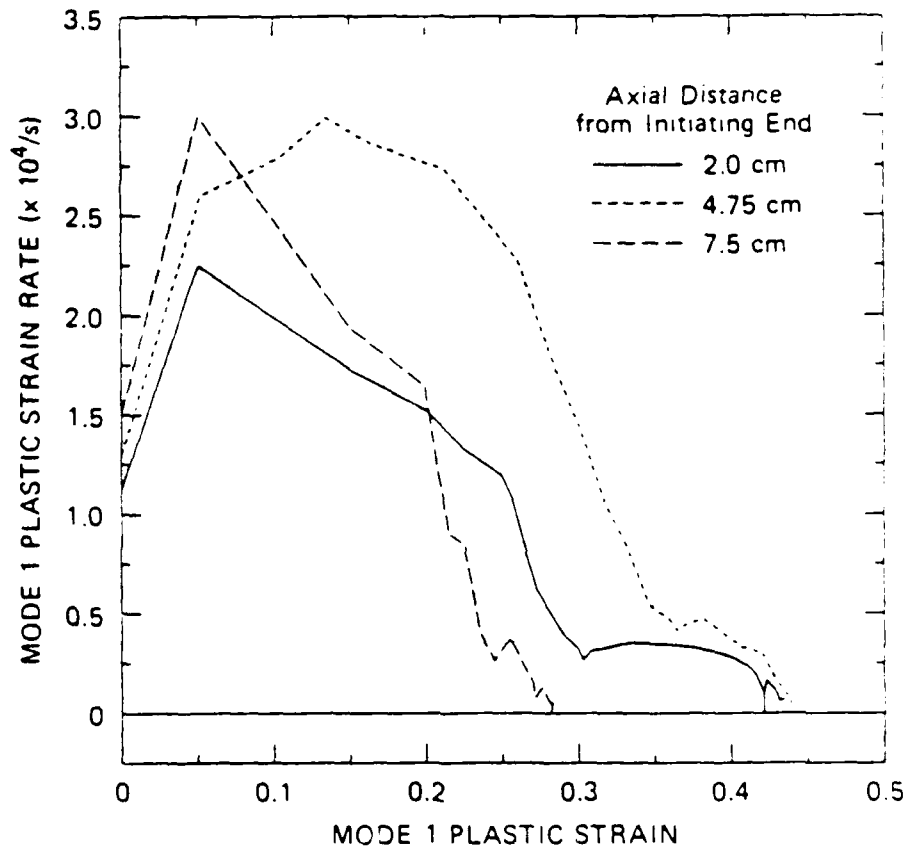
MA-7893-199

FIGURE 29 CALCULATED PLASTIC STRAIN HISTORIES FROM 4340 STEEL TEST 8



MA-7893-203

FIGURE 30 CALCULATED PLASTIC STRAIN RATE HISTORIES FOR RHA TEST T-9



MA-7893-204

FIGURE 31 CALCULATED PLASTIC STRAIN RATE VERSUS STRAIN FOR RHA TEST T-9

$$N_g = N_0 \exp(-R/R_1),$$

where N_g is the number of shear bands per unit volume with radii greater than R , N_0 is the intercept at zero radius, and R_1 is a shape parameter for the distribution. N_0 and R_1 are determined in the fitting process. These numbers, which thus characterize the damage in the CFC experiments, are shown in the "Data" columns in Table 5 for both RHA and 4340 steel.

Determination of Parameters

There are 13 parameters provided for describing shear banding kinetics in SHEAR3. All must be specified, but not all are critical for controlling the damage development. These parameters are listed and briefly defined in Table 6. Some nominal values for steels are also given. (A more complete description is in Volume II of this report.) In the following two subsections, we will explain how numeric values are determined for these parameters from CFC data.

The first two parameters, B_1 and B_2 , govern growth and nucleation and must be determined by fitting the number and size data from cylinder experiments, accounting for the imposed strain histories. The fitting procedure is described in the next subsection. B_3 , the nucleation size parameter (R_n), is estimated by extrapolating R_1 , on a graph of R_1 versus plastic strain, back to the nucleation threshold strain (B_5 , to be described). For the RHA and 4340 steel data considered here (as shown in the "Data" columns in Table 5), it was difficult to make an accurate extrapolation because of the relative sparseness of data in the intermediate damage range. However, $B_3 = 0.01$ cm appears to fit the data well.

B_4 is the thermal diffusivity, which equals the thermal conductivity divided by the density and the specific heat at constant pressure. The nominal value for steel is 0.146/s. B_5 is the nucleation threshold strain. It is first estimated by comparing the level of damage and peak plastic strains attained for a series of CFC tests (for example, comparing damage in Table 5 and the strains in Figures 25 through 27 for RHA).

Table 5

SHEAR BAND DAMAGE CHARACTERIZATION PARAMETERS FOR RHA
AND 4340 STEEL FROM CFC DATA AND C-HEMP SIMULATIONS

Material	Test	Axial Position*	Data		Simulations	
			N _o	R _l	N _o	R _l
RHA	T-2	2.0	Only incipient shear band damage present		none none 0.5 0.013	
		4.75				
		7.5				
RHA	T-9	2.0	130	0.038	118	0.046
		4.75	290	0.047	193	0.044
		7.5	none		none	
RHA	T-10	2.0	120	0.040	145	0.047
		4.75	270	0.049	240	0.046
		7.5	5	0.026	none	
4340 Steel (R _c 40)	2	5.6	3	0.04	28	0.070
9.4		60	0.07	71	0.087	
11.9		2	0.08	21	0.054	
4340 Steel (R _c 40)	8	5.4	70	0.10	31	0.074
9.2		90	0.10	83	0.098	
11.7		70	0.10	50	0.097	

*Distance in cm from initiating end of CFC tube.

Table 6

SHEAR BANDING KINETICS PARAMETERS IN SHEAR3

<u>Parameter</u>	<u>Values*</u>	<u>Definition</u>
B ₁	40	Growth coefficient in equation $dR/dt = B_1 R d\epsilon/dt$, where R, ϵ , and t are shear band radius, time, and plastic strain, respectively
B ₂	1 cm ⁻³	Nucleation coefficient
B ₃	0.01 cm	Nucleation size parameter, R _n
B ₄	0.146 s ⁻¹	Thermal diffusivity
B ₅	0.3	Nucleation threshold strain
B ₆	0.07	Relative maximum shear distortion associated with a band
B ₇	0.04 cm	Maximum shear band radius at nucleation
B ₈	1.0	Fragment shape parameter in equation $V_v = B_8 (R_f)^3$, where V _v and R _f are the void volume and fragment radius, respectively
B ₉	0.6	Tangent of the internal friction angle used in computing shear resistance on shear band slip planes
B ₁₀	2	Plastic strain storage indicator
B ₁₁	1.0	Damage indicator for triggering slide lines
B ₁₂	0	Currently unused
B ₁₃	8	Number of radii used for each shear band size distribution

*Nondimensional unless otherwise specified.

The fitting procedure described below is then used to get a more accurate value.

B_6 is the relative maximum shear distortion associated with a band. It is determined by sectioning a recovered CFC tube perpendicular to its axis (for Mode I bands) and measuring the ratio of the peak shear displacement and the peak band depth in the slip plane (B/d in Figure 8). The nominal value of 0.07 was taken from previous measurements on HF-1 and 4340 steels.^{12,14}

B_7 is the maximum shear band size at nucleation. This parameter may be determined by observing the largest bands at very small amounts of strain. The primary effect of this parameter is to determine the resolution in the size distribution for the calculations; therefore, B_7 should be several times as large as R_n . Here we chose a value of 0.04.

The fragment shape parameter, B_8 , was chosen to be 1.0 to indicate relatively bulky or equiaxed fragments. B_9 is the tangent of the angle of internal friction; in the absence of other data, an angle of 30° was used. The remaining parameters, B_{10} through B_{13} , were chosen to make all planes active, and to give a reasonably fine discretization of the size distribution.

Fitting Procedure

In this section, we discuss the method we used to evaluate the most critical shear band kinetics parameters (B_1 , B_2 , and B_5) to provide the best match to the observed damage. To perform the simulations of shear banding under an arbitrary imposed strain histories, we developed a small computer program, NUCLEAT. This program is basically a simplification of SHEAR3. NUCLEAT contains input procedures for material and shear band properties, nucleation and growth processes for a single band orientation, and the logic to follow a prescribed strain path.

To perform a simulation for a single axial position in one of the CFC specimen tubes, we estimated a complete set of shear banding parameters and inserted the strain history computed from a no-damage

C-HEMP calculation (such as those in Figures 25 through 29). The initial NUCLEAT simulation yielded a set of $N_0 - R_1$ values appropriate to these parameters. Based on these results we could estimate a new set of parameters and repeat the calculation. This iterative process was accelerated by simultaneously performing NUCLEAT simulations for all of the relevant positions in all of the CFC experiments on a particular material (e.g., all six 4340 steel points or all nine RHA points considered here).

The end result of the iterative process using NUCLEAT was a set of shear banding kinetics parameters that simultaneously gave a best match to all data sets for a single material. The parameters obtained for RHA and 4340 steel are listed in the row labeled SHEAR3 in Table 7 (we have also included in this table the EP model parameters that govern the homogeneous plastic deformation of the material before and during shear banding). The N_0 and R_1 values obtained from the NUCLEAT calculations using these parameters are shown under "Simulations" in Table 5. The correspondence between the measured and simulated N_0 and R_1 values is certainly not precise, but probably within material variability (the variability of material damage values is expected to be much higher than that for yield strength, moduli, and other macro parameters). We feel that the agreement is good enough to indicate that the growth and nucleation functions have forms that reasonably well represent the actual processes.

The next step in generating and verifying a set of shear banding kinetics parameters for a material is to perform complete simulations of the CFC tests, using C-HEMP with the SHEAR3 parameters obtained from the NUCLEAT calculations. The computed damage from such simulations would be expected to differ from the NUCLEAT results, especially for cases of high damage, because the developing damage calculated by SHEAR3 affect the stresses and therefore the subsequent strains in the C-HEMP simulation. (In contrast, in the NUCLEAT calculations, the imposed strain histories were based on no-damage or low-damage simulations.) Unfortunately, we had insufficient time and funds to perform these C-HEMP simulations, so the listed parameters must be considered preliminary.

Table 7

SHEAR3 AND EP MODEL PARAMETERS

Model	Parameter Type	4340 Steel R_{e40}	RHA	
SHEAR3	Shear	60.0	20.0	
	banding	1.0	2.0	
	kinetics	0.01	0.01	
	parameters:	B_1	0.146	0.146
		B_2	0.24	0.35
		B_3	0.07	0.07
		B_4	0.04	0.04
		B_5	1.0	1.0
		B_6	0.577	0.577
		B_7	2.0	2.0
		B_8	2.0	2.0
		B_9	0.0	0.0
		B_{10}	8.0	8.0
EP	Yield Strength (Kbar)	10.3	6.8	
		10.7	7.7	
		13.7	8.7	
			9.5	
			10.4	
			11.1	
EP	Equivalent plastic strain	0.0	0.0	
		0.03	0.02	
		1.0	0.07	
			0.12	
			0.17	
			0.27	
	0.47			
	1.3			

V COMPUTER SIMULATION OF ARMOR PENETRATION

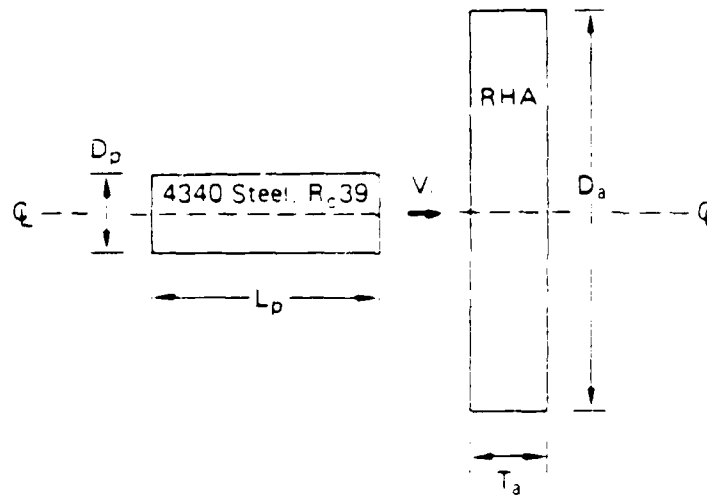
A series of armor penetration simulations, involving impact velocities both near and well above the ballistic limit, were performed using the newly developed C-HEMP code. There were three primary purposes for these calculations. The first was to test some of the capabilities of C-HEMP (in particular the slide line and rezoning features) under the extreme deformation conditions that exist in a penetration scenario. The second was to study the effect of the inclusion of the SHEAR3 damage model upon the penetration simulations. And the third was to compare, at least qualitatively, the simulated results with the results of previously performed experiments having a similar geometry and impact velocity.

All of the simulations involved the normal impact of a cylindrical 4340 steel ($R_c 40$) penetrator into a circular RHA plate, a scenario for which we have a large experimental data base. The geometry and impact velocity (V_i) for the five simulations that will be discussed in this section are shown in Table 8 and Figure 32. Simulations No. 1 and 2 represent the case of a long-rod penetrator impacting at well above the ballistic limit. The corresponding experiment was performed at the BRL quarter-scale facility during the second year of this program¹⁵ and is depicted in Figure 33. Simulations No. 3, 4, and 5 represent the case of a shorter penetrator near or below the ballistic limit. The corresponding experiments were performed at SRI International during the first year of this program,¹⁵ and the results are depicted in Figure 34.

The cylindrical symmetry of the normal penetration scenario allows the two-dimensional C-HEMP code to be used in its axisymmetric mode. A sample initial cell layout is shown in Figure 35. Each quadrilateral cell actually represents the toroidal volume obtained by rotating that cell around the centerline (axis of symmetry). A slide line extends along the impact interface, allowing the end of the penetrator to slide without friction along the front face of the armor.

Table 8
C-HEMP PENETRATION SIMULATIONS

No.	Impact Velocity, V, (m/s)	Dimensions (cm) (see Figure 32 below)				Constitutive Model Used in Simulation	Figures Showing Results
		D_p	L_p	D_a	T_a		
1.	1550	1.02	10.2	15.24	2.54	SHEAR3	36 and 39
2.	1550	1.02	10.2	15.24	2.54	EP	39
3.	750	0.635	1.27	7.62	0.635	SHEAR3	37 and 40
4.	750	0.635	1.27	7.62	0.635	EP	40
5.	500	0.635	1.27	7.62	0.635	SHEAR3	38



MA-7893-195

FIGURE 32 CROSS-SECTIONAL GEOMETRY FOR PENETRATION SIMULATIONS



FIGURE 33 RADIOGRAPHS TAKEN 30, 145, AND 285 μ s AFTER 1.55 km/s IMPACT OF A 4310 STEEL (R-40) ROD ON TO AN RHA TARGET PLATE

Both back scatter and clover-leaf fragments are seen. The penetrator travels from right to left.

Shear Banded
Projectile Nose
Fragments



1/4"

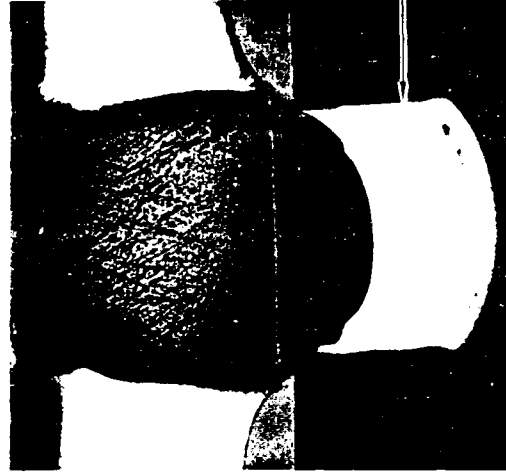
(a) 655 m/s

Shear
Banded
Penetrator
Nose
Fragments



1/4"

(b) 710 m/s



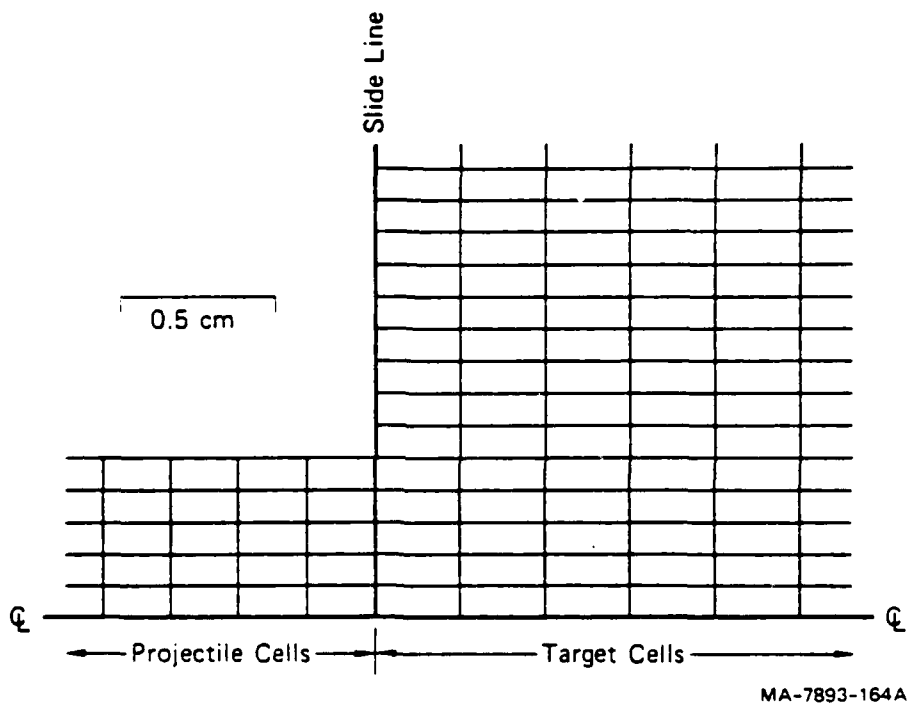
1/4"

Plug

(c) 792 m/s

MA 7893 121A

FIGURE 34 CROSS SECTIONS THROUGH CENTERS OF RHA TARGETS IMPACTED BY 4340 STEEL (R-40) PROJECTILES



MA-7893-164A

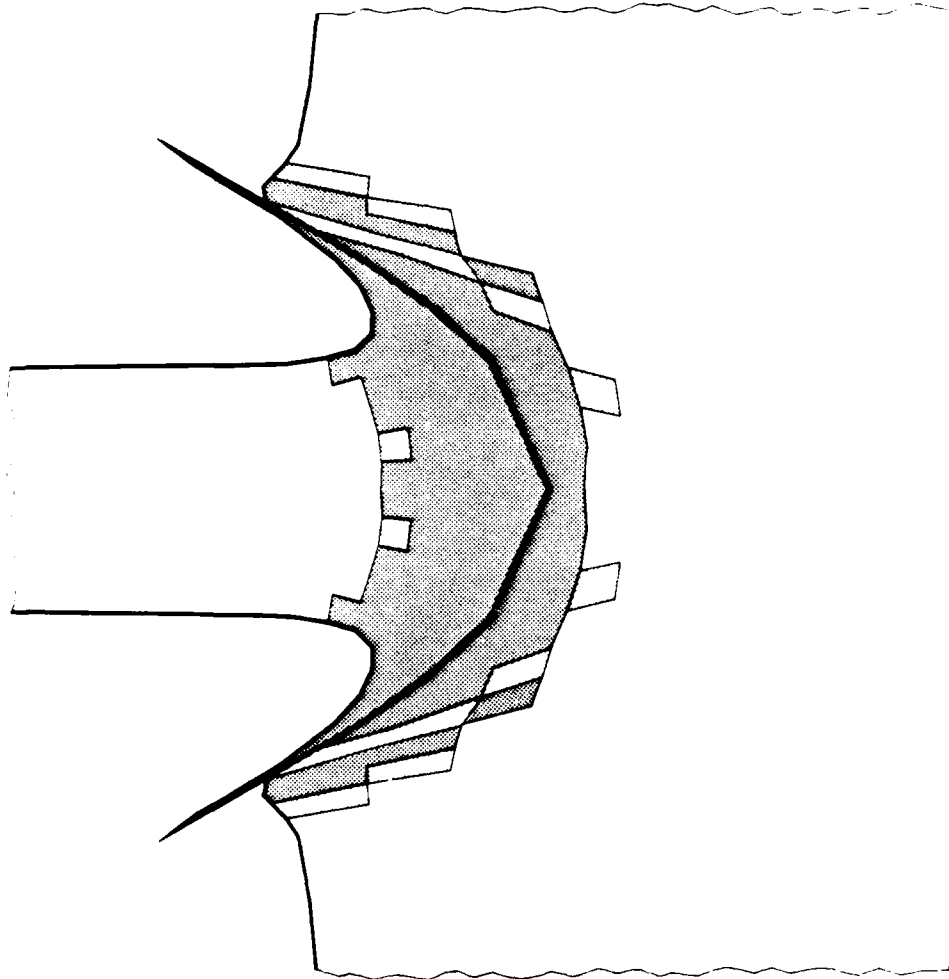
FIGURE 35 PORTION OF ORIGINAL CELL LAYOUT FOR PENETRATION SIMULATIONS

The cells in the vicinity of the impact interface are subject to severe shear deformations, and because the time step (the time interval between successive computational cycles) must be less than the time for an incremental stress wave to propagate across any cell, the time step decreases precipitously, thus ending the calculation.

We have used a three-part strategy to mitigate this effect. First, all of the cells in the vicinity of the impact interface are continuously rezoned. Second, the cells are allowed to collapse into triangles; if one node of the quadrilateral is close to penetrating one of the opposite sides, that node is held fixed in the direction perpendicular to the side it is about to penetrate, and that node is eliminated from the time step calculation. Third, as a last resort, any cell whose calculated time step falls below a user-specified value is eliminated from further calculational cycles. As a result, subsequent motions and deformations in the vicinity of such a cell will be erroneous, but there should be little deleterious effect on regions far removed.

The SHEAR3 model (which is described in detail in Volume II of this report) was used for both the armor and penetrator materials in three of the simulations (Nos. 1, 3, and 5) to calculate the nucleation, growth, and coalescence of shear bands, and the resultant loss of shear strength. The shear banding kinetics parameters used in SHEAR3 were obtained from previous CFC experiments and computational modeling (as described in Section IV), and are listed in Table 7.

Figure 36 shows the shear band damage profile for simulation No. 1 ($V_1 = 1550$ m/s with SHEAR3) at $11.1 \mu\text{s}$ after impact, which is as far as the calculation proceeded before the time step became excessively small. The projectile has penetrated about 40% of the way into the target, while the back surface of the target has experienced only very small motions. The kinetic energy of the projectile is still approximately 88% of its original value. The pointed projectile tip is probably a result of insufficient computational cell resolution in the radial direction in the penetrator. A simulation with better resolution exhibited less of a pointed tip, but resulted in earlier time step degradation.



MA-7893-174

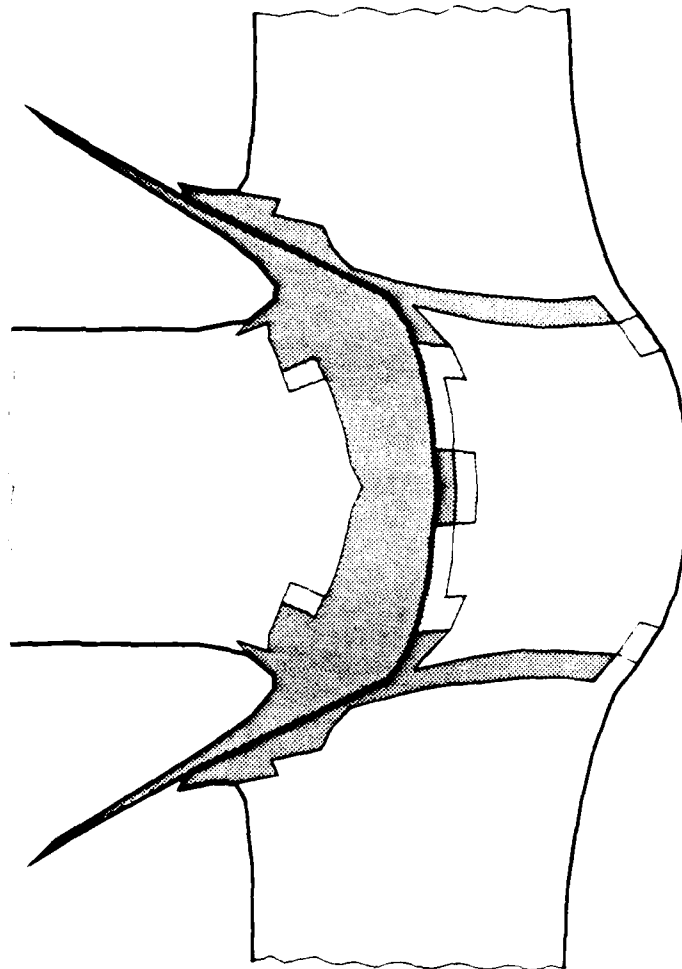
FIGURE 36 PROFILE OF SIMULATION NO. 1 ($V_i = 1550$ m/s) $11.1 \mu\text{s}$ AFTER IMPACT

Dark shaded regions indicate computational cells that are completely damaged by shear banding. Light shaded regions indicate cells that have experienced some shear banding failure.

The dark shaded regions in Figure 36 (and in subsequent figures) represent cells that have been completely damaged by shear banding and thus no longer retain any shear (or tensile) strength. The lighter shaded regions represent cells that have undergone partial shear banding damage. The damaged region occupies the impact end of the projectile as well as a broad, relatively uniform region of the target adjacent to the impact zone. From the progression of damage at times less than $11 \mu\text{s}$ and from the relatively small loss of projectile kinetic energy at $11 \mu\text{s}$, one can roughly extrapolate the progression of damage at later times. It appears that the entire thickness of the target plate in the vicinity of impact will become fully damaged, while the projectile still retains a large fraction of its kinetic energy, thus reasonably well simulating (at least qualitatively) the large volume of small fragments observed in Figure 33.

Figure 37 shows the damage profiles for simulation No. 3 ($V_1 = 750 \text{ m/s}$) $12.3 \mu\text{s}$ after impact. The projectile has penetrated 60% of the way into the target, the back surface of the target has moved about 40% of its thickness, and the kinetic energy of the projectile has dropped to 38% of its original value.

The damaged region in the projectile is similar to that for the higher velocity simulation. But in the target the situation is quite different. Rather than occupying a broad region adjacent to the impact zone, the fully damaged area localizes along a narrow band (one cell thick) extending toward the back of the plate. The band's distance from the impact axis is slightly greater than the projectile radius. From the progression of damage at earlier times and from the remaining projectile kinetic energy, it is clear that a continuation of the simulation (if the time step would have permitted it) would show the damage band reaching the back surface of the target and forming a plug. The plug and the remainder of the target would be largely undamaged by shear banding, a result similar to that seen experimentally for a 792 m/s impact [Figure 34(c)].



MA-7893-175

FIGURE 37 PROFILE OF SIMULATION NO. 3 ($V_i = 750$ m.s) $12.3 \mu\text{s}$ AFTER IMPACT

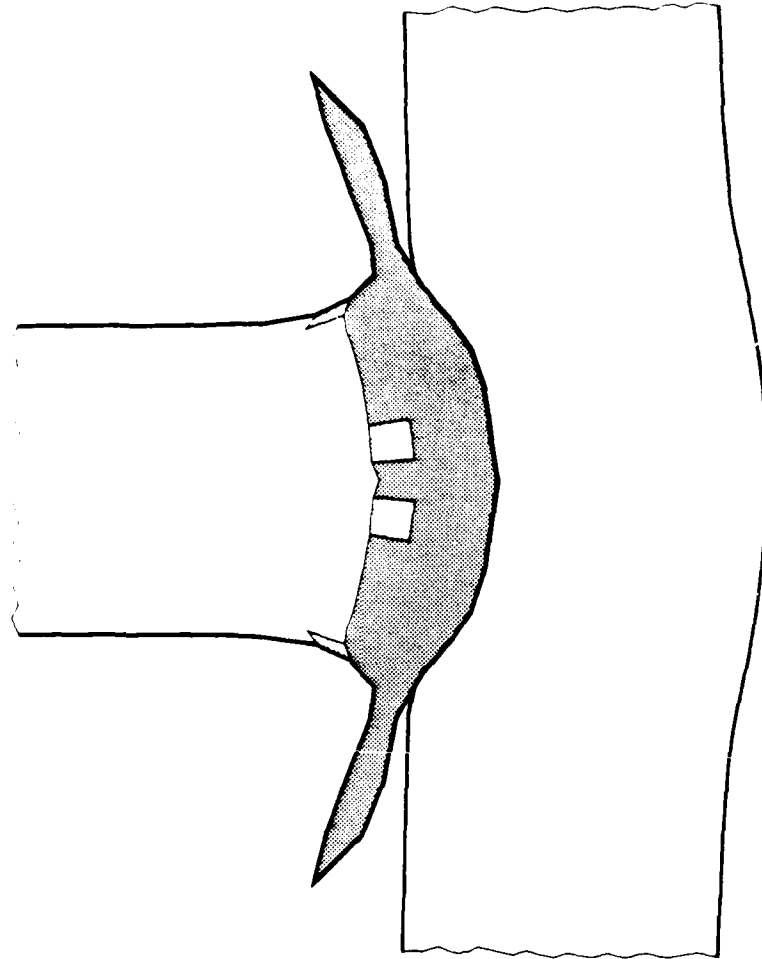
Dark shaded regions indicate computational cells that are completely damaged by shear banding. Light shaded regions indicate cells that have experienced some shear banding failure.

Figure 38 shows the damage profile for simulation No. 5 ($V_i = 500$ m/s) at 12.5 μ s after impact. The front of the projectile is fully damaged by shear banding, but the target has undergone insufficient strains to nucleate any shear bands. The projectile has penetrated 30% of the way into the target, the back surface of the target has moved about 1/6 of its thickness, and the projectile kinetic energy is only 21% of its original value. It is therefore unlikely that a continuation of the calculation would produce any significant shear banding in the target; the final profile would appear similar to that of the experimental 655 m/s impact [Figure 34(a)].

These lower impact velocity simulations qualitatively predict the progression of damage we have observed in a target in the vicinity of the ballistic limit—from homogenous plastic deformation, to shear strain localization, to complete plugging. In addition, the calculations support our experimental finding that the ballistic limit for this particular geometry is between 710 and 792 m/s.* However, considering the large cell size and the preliminary nature of the shear banding parameters used in the calculations, it was not expected that we would accurately predict a ballistic limit. What is significant here, we believe, is the ability of the simulations to correctly predict, using the same damage model and kinetics parameters, the qualitative difference between the penetration phenomenology observed at the two widely separated impact velocity regimes.

To more fully assess the impact of the SHEAR3 damage model on the simulated penetration at velocities both near and well above the ballistic limit, we repeated two simulations replacing SHEAR3 with the elastic-plastic (EP) model (Nos. 2 and 4). The EP model allows homogeneous shear deformation along a work-hardening yield curve, but no shear banding. The EP model parameters, determined from quasi-static

*The ballistic limit is a statistical quantity and can be determined only from many tests.



MA-7893-176

FIGURE 38 PROFILE OF SIMULATION NO. 5 ($V_i = 500$ m/s) 12.5 μ s AFTER IMPACT

Dark shaded regions indicate computational cells that are completely damaged by shear banding. Light shaded regions indicate cells that have experienced some shear banding failure.

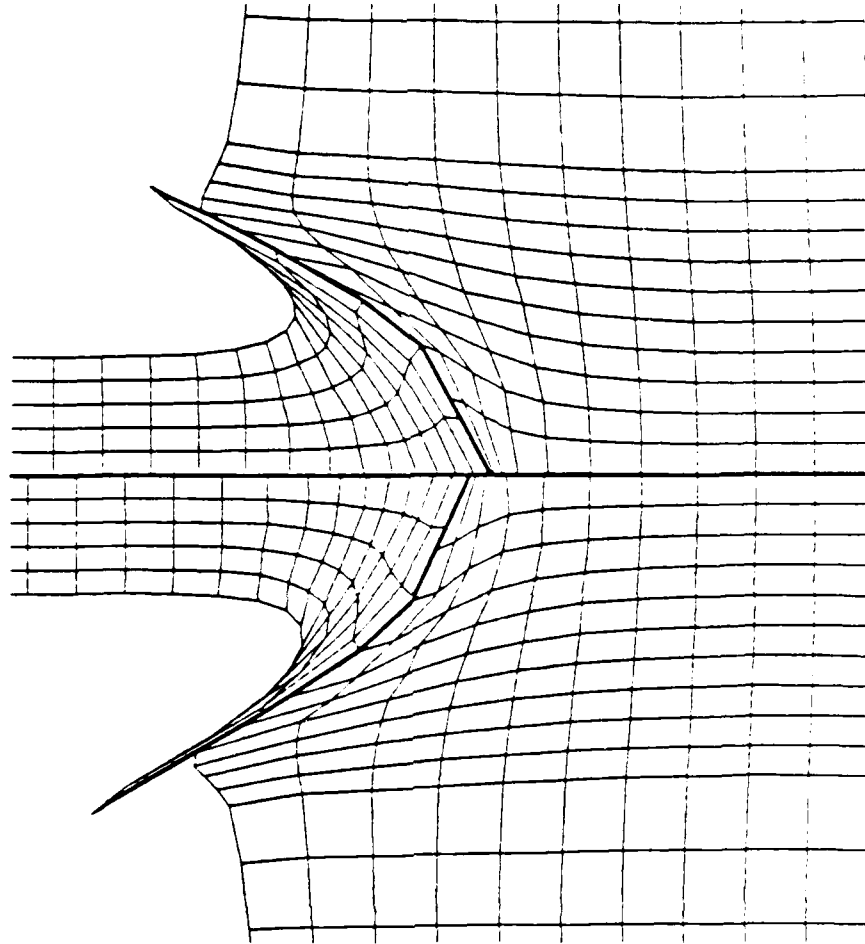
tensile tests, are also listed in Table 7 in terms of yield strength as a function of equivalent plastic strain. The constitutive paths described by the SHEAR3 and EP models are identical before the onset of shear banding. Comparisons between simulations using SHEAR3 and otherwise identical simulations using the EP constitutive model are described below.

For the higher velocity simulations ($V_i = 1550$ m/s), there appears to be no significant difference in the cell profiles at about 11.5 μ s after impact (see Figure 39). Simulation No. 1, using SHEAR3, resulted in slightly greater deformation of both the projectile and target in the region near the impact interface, and slightly less penetration, than simulation No.2, using EP.

There was no significant difference in the simulated deformations occurring early in a high-velocity penetration scenario between models having different yield and shear failure algorithms. This is not surprising because the early stresses are very high compared with the yield strengths, and thus the compressibility and momentum relations largely govern the deformations. Of course, only SHEAR3 can model the actual shear band failure processes and the resultant reduction in shear strength, and therefore be able to predict deformations later in the penetration (when material strengths play a more important role), as well as fragmentation.

For the lower velocity simulations ($V_i = 750$ m/s), large differences in deformation do occur in the first 12 μ s after impact (see Figure 40). Simulation No. 3, using SHEAR3, resulted in far greater deformations in the impact region for both the projectile and target than simulation No. 4, which used EP. More significantly, the simulation using EP did not experience any of the localization of shear damage discussed above (and shown in Figure 37), which would eventually lead to a plugging type of target failure. As a result, the projectile penetration and the target back surface deflection are about 25% smaller in simulation No. 4 than in simulation No. 3.

Upper Profile — Simulation No. 2 (with EP model), 11.9 μ s after Impact

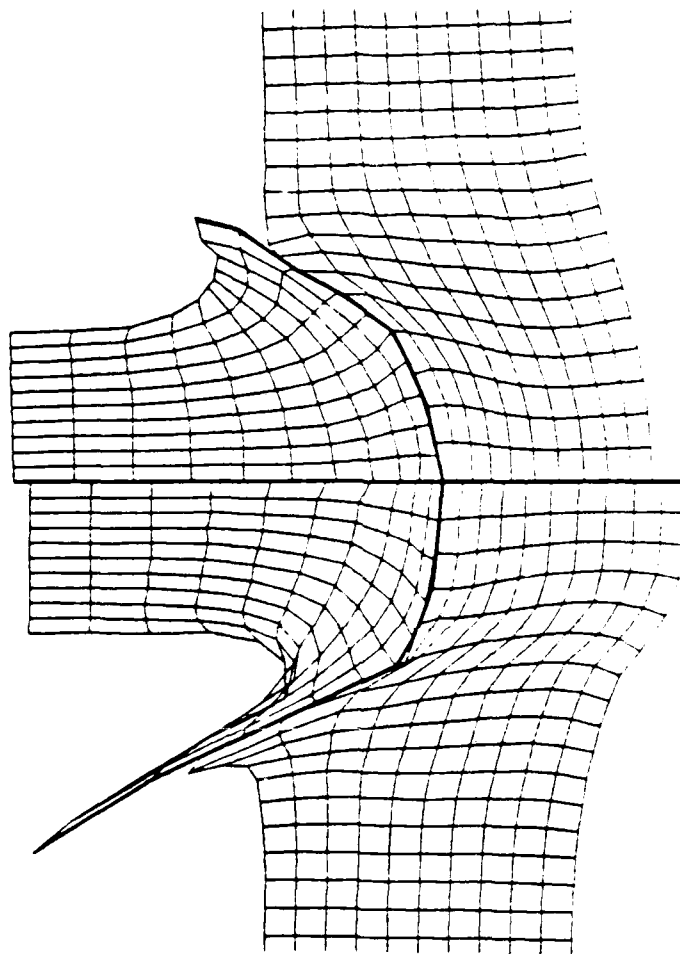


Lower Profile — Simulation No. 1 (with SHEAR3 model), 11.1 μ s after Impact

MA-7893-196

FIGURE 39 EFFECT OF SHEAR BANDING DAMAGE ON SIMULATED PENETRATION
AT AN IMPACT VELOCITY OF 1550 m/s

Upper Profile — Simulation No. 4 (with EP model), 12.5 μ s after Impact



Lower Profile — Simulation No. 3 (with SHEAR3 model), 12.3 μ s after Impact

MA-7893-197

FIGURE 40 EFFECT OF SHEAR BANDING DAMAGE ON SIMULATED PENETRATION
AT AN IMPACT VELOCITY OF 750 m/s

In conclusion, although we have not been able to simulate to completion an armor penetration by projectile impact, we have, by use of the C-HEMP code with the SHEAR3 model, extended the simulation sufficiently to demonstrate that it can predict, at least qualitatively, much of the armor penetration phenomenology that we have observed experimentally.

VI RECOMMENDATIONS FOR FUTURE WORK

As documented in this report, SRI International has made significant progress in developing a phenomenologically sound, material-property-based computational method for predicting armor penetration by projectile impact. At this point, the method can be used to simulate moderately deep penetrations caused by normal impact of long-rod projectiles, and to correctly predict the mode of penetration as well as rough estimates of the resultant fragment size and velocity distributions. However, much needs to be done to extend the method to deep penetrations and oblique impacts, and to make it readily useable by DoD personnel to facilitate the design of new armor, penetrator, or fragmentation systems. In this chapter we present our recommendations for achieving this goal.

The basic aim of the future work we are recommending is to improve, simplify, and transfer to BRL an improved capability for computationally predicting armor penetration and the resultant fragment size, shape, and velocity distributions. The approach we suggest is as follows:

- Determine what modifications can be made to the shear band model, the computer code (C-HEMP), and the experimental procedures for characterizing a material, to improve accuracy, facilitate use, and extend the capability to deep penetrations and oblique impacts.
- Implement these modifications, testing their effectiveness by computational simulations of previously performed penetration experiments.
- Apply the computational method, with the modifications, to the predictions of various penetration (or other appropriate) scenarios of interest to BRL.
- Document the model, the code, and the procedures for material characterization, and transfer this capability to BRL in a manner that will make it readily available for use in design calculations.

All modifications to the computational method would remain within our overall philosophy of basing the model on a quantitative description of the phenomenological processes that do occur in an actual penetration. We can thus be assured that the model will be applicable to arbitrary geometries.

We have divided the recommended future work into six suggested tasks, which are described below.

Task 1: Refinements to Shear Band Model

Examination of experiments involving both normal and oblique impact of long-rod penetrators into RHA plates¹⁶ have revealed several phenomenological features that are either not yet incorporated in our shear banding model, or if incorporated, have not been fully tested or exercised. These features include the significance of shear band anisotropy to the penetration and fragmentation process, tensile separation along an already-formed shear band, and the possibility that a specific point in a material may begin to fail by tension before it has experienced sufficient shearing to form shear bands. The last feature is extremely important in fragmenting rounds, but may also be important in penetration scenarios in which tensile failure in the target precedes plug formation.

SRI International has recently been developing, primarily under another program,* a model for shear banding in an anisotropic material, SHEAR4, which describes the nucleation and growth of bands in as many as seven distinct orientation modes. This model is anisotropic: it relaxes shear stresses and reduces shear strengths only on the specific planes that are undergoing shear banding, and it allows for different nucleation and growth parameters for different planes (to account for material anisotropy). It also allows the shear bands of a particular orientation mode to change direction as their cell deforms.

*Army Research Office Contract DAAG29-81-K-0001

ND-R198 757

COMPUTATIONAL MODEL FOR ARMOR PENETRATION(U) SRI
INTERNATIONAL MENLO PARK CA D C ERLICH ET AL OCT 87
BRL-CR-586 DAAK11-78-C-0115

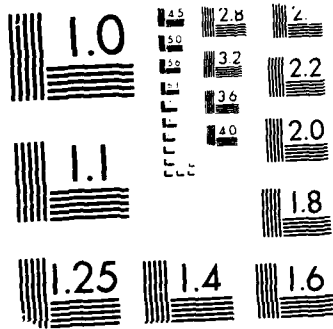
2/2

UNCLASSIFIED

F/G 19/4

NL





MICROCOPY RESOLUTION TEST CHART
NATIONAL BUREAU OF STANDARDS-1963-A

of the bands in the other orientation modes. However, these anisotropic capabilities have not been fully tested or exercised.

There exists, from the current program (see Section III), CFC data on RHA tubes whose axes have been cut parallel to and perpendicular to the rolling plane. Up to now, we have only considered orientation Mode 1 bands when attempting to computationally simulate the experiments. We now recommend testing the ability of the code to predict shear banding in other than Mode 1 orientations, using the parameters determined from Mode 1 simulations in the two directions. This would provide a fuller check on the anisotropic capabilities of SHEAR4.

Furthermore, in all previous simulations using either of our two shear banding models, a specific computational cell is allowed to nucleate and grow shear bands but not tensile voids, even if the stress and strain history for that cell warrants initial tensile failure. For scenarios that include simultaneously both shear banding and tensile failure (e.g., fragmenting rounds), the programmer must specify in advance which cells will follow the shear banding model and which will follow a tensile failure model. We therefore recommend examining the possibility of having each cell determine, from its loading history and material failure properties, what type of failure it undergoes, and switch from one type to another if the loading changes appropriately. If this feature appears to be feasible, we recommend implementing it in the SHEAR4 model and testing it against existing experimental data.

From phenomenological experiments, we have seen that armor and penetrator fragmentation is, in most cases, caused by the intersection of shear bands propagating in different directions. In our current shear banding models, fragmentation in a particular computational cell is said to have occurred when a damage parameter (a simple function of the density and size of the shear bands in that cell) reaches unity. The resultant fragment size distribution comes from the final shear band size distribution before fragmentation (many small bands produce many small fragments, while a fewer and larger bands produce fewer and larger fragments).

However, no attempt is made to describe the shape or aspect ratio of these fragments, although pertinent information is available, in terms of the size distributions of the shear bands in the various orientation modes present within that cell. For example, if there are similar distributions of bands in several different orientations, then chunky fragments (aspect ratio nearly unity) might be expected. But if one orientation had a much lower density of bands, then elongated fragments (large aspect ratios) might be expected. We therefore recommend exploring methods of improving the simple damage parameter determination of cell fragmentation and implementing a fragment shape prediction capability in the SHEAR4 model.

Task 2: Improvements to C-HEMP for Armor Penetration Calculations

The current version of C-HEMP incorporates many of the features considered important for armor penetration calculations. The finite element cell numbering scheme, which makes cell numbering independent of cell location, allows more flexibility for slide line insertion or separating (and eliminating) spalled regions. The capability to handle complex material models makes it possible to use SHEAR3, SHEAR4, and other MSFM models, such as the NAG ductile and brittle failure models, as well as any new models to be developed in the future. The current slide line capability allows slip (with or without a frictional component) along user-located slide lines that are either already "unzipped" or "unzip" as the computation proceeds. And the automatic rezoner compensates, to a certain extent, for the large cell distortions involved in a penetration simulation.

However, the main problem with C-HEMP is its inability to complete deep penetrations simulations because extreme cell distortions decrease the allowable time step to unworkably small values. The usual solution to this problem is to replace quadrilateral cells with triangular cells. While the triangular cells' resistance to collapse (as compared to a quadrilateral cell, in which one node may collapse onto an opposite side) may in some situations cause unrealistically high pressures, it

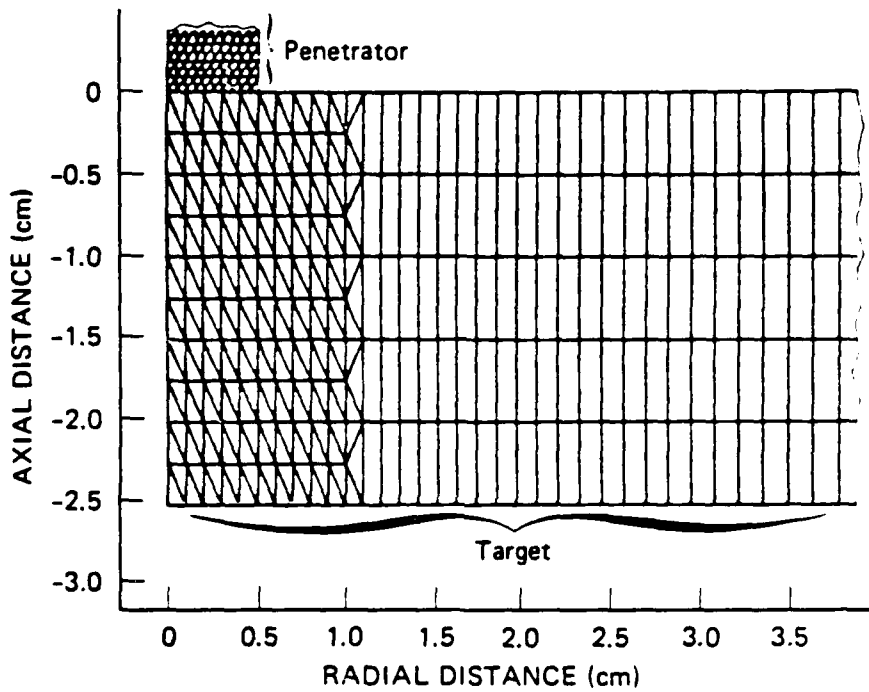
keeps the time step reasonably large and thus allows the calculations to proceed to conclusion. We expect that the excessive pressures will be less of a factor in the primarily shear-strain-driven shear banding models than in the primarily pressure-driven pore compaction model, for example.

What appears to be most promising is a mixed approach whereby both triangular and quadrilateral cells are used in the same calculation: the triangular cells are used in the regions of expected extreme deformations. Such an approach was used for a deep penetration simulation with the SWE2D code,* as shown in Figures 41 and 42. Of course, this code does not include SHEAR3 and thus cannot predict plugging or fragmentation, but it can handle extreme cell deformations (similar results have been obtained with other triangular cell codes, such as BRL'S EPIC code). Combining a triangular cell capability with the shear banding models and other features currently in C-HEMP would be the next logical step toward completing a computational method for predicting deep penetrations.

In addition to the mixed triangular and quadrilateral cell feature, a more complex slide line capability is needed to better simulate both normal and oblique impacts. For normal impacts of long-rod penetrators at velocities somewhat greater than the ballistic limit of the armor plate, penetration occurs by the propagation of a shear band across the thickness of the armor plate to form a plug. When this band reaches the back surface of the armor, the plug is removed.

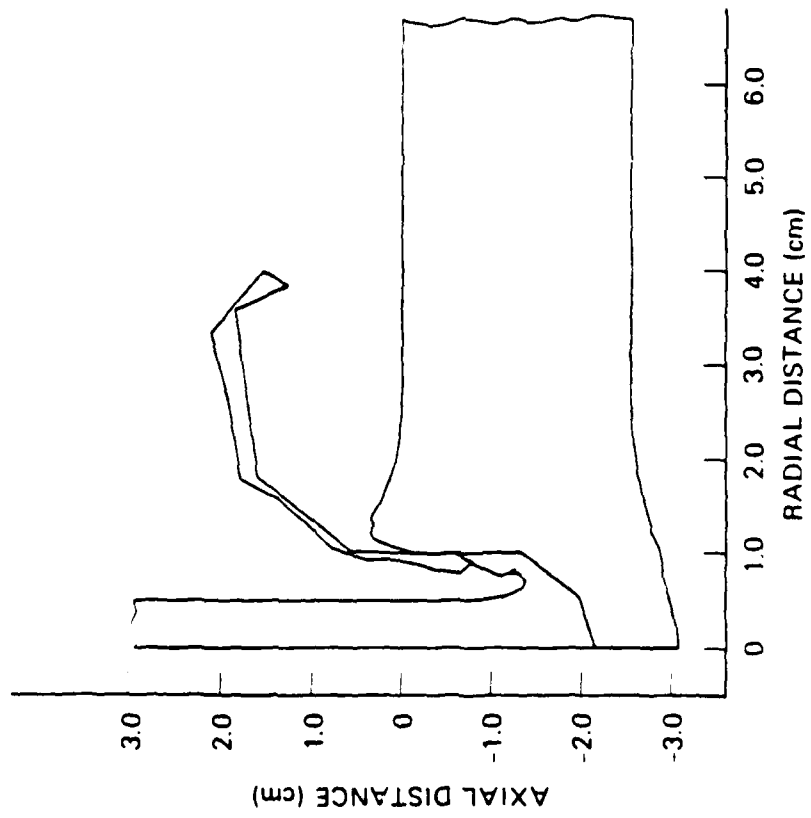
One method of computationally simulating this scenario is to insert a slide line at an appropriate position between two rows of armor plate cells parallel to the direction of impact. This slide line is initially inactive, but is gradually activated along its length by a criterion related to that of nucleation and growth in our shear band model.

*Written by Thomas Cooper at the Swedish Detonic Institute.

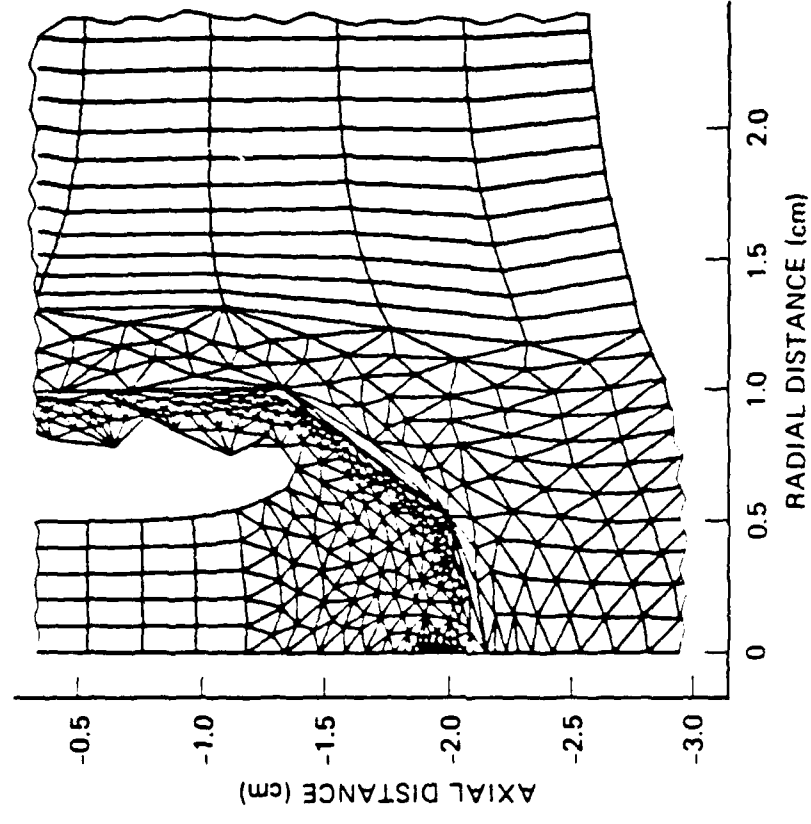


MA-7893-207

FIGURE 41 INITIAL CELL PROFILES FOR SWE2D DEEP PENETRATION SIMULATION, USING COMBINATION OF TRIANGULAR AND QUADRILATERAL CELLS



(a)



(b)

MA-7893-208

FIGURE 42 COMPUTATIONAL PROFILE (a) 30 μ s AFTER START OF SWEZD DEEP PENETRATION SIMULATION, AND DETAIL (b) OF HIGHLY DEFORMED REGION

Another level of slide line complexity arises because the location of the unzipping slide line cannot necessarily be determined in advance of the computation. If a blunt-nosed hardened penetrator impacts normally into a 4340 steel (R_c40) armor plate, for example, a shear band nucleates in the armor at the very edge of the penetrator, forming a plug with the same diameter as that of the penetrator. For this case, the slide line can be user-located in advance. However, for a round-nosed penetrator or for a more realistic armor material, such as RHA, significant material distortion may occur in both the armor and penetrator before the nucleation of a shear band in the armor, and plugs have been formed with a diameter significantly greater than that of the penetrator.¹⁵

It would thus be desirable to have the code select the position of the slide line as the calculation progresses. This "self-locating" slide line could be positioned by the code adjacent to the first cell that satisfies a shear banding damage criterion that corresponds to nearly complete loss of shear strength in the direction of the slide line. Implementing this feature should be relatively straightforward, since the finite element numbering scheme would allow for creating extra cell nodes as required by adding a slide line in the middle of a calculation. Once the slide line is positioned, it would proceed to unzip from node to node as the cells adjacent to the nodes satisfy the same damage criterion.

Not only is the self-locating unzipping slide line more realistic from a phenomenological viewpoint and requires less user intervention, but it has a third advantage. As described in Section V, simulations of normal rod impacts without the use of slide lines have resulted in the localization of shear banding damage in a particular row of cells parallel to the impact direction. The ensuing loss of shear strength causes these cells to undergo extreme shear distortions, significantly reducing the time step between cycles and thereby greatly increasing the

calculation time. A self-locating slide line would alleviate this problem, and allow for complete simulation by letting the plug separate from the target.

We have thus far assumed that the lateral surfaces of the plug are relatively straight and perpendicular to the armor plate. Such is not the case in many armor penetration scenarios. During normal impact at velocities below or slightly above the ballistic limit, the shear bands that form the lateral edges of the plugs turn inward (toward the penetrator axis) as they grow toward the back of the armor.²⁹ And during oblique impact, the penetrator may, as it proceeds through the target plate, rotate to an orientation more normal to the target face. So the hole formed by the plug, or the fragmented material removed, has surfaces with curvatures that are certainly not predictable.

We are thus led to a further level of slide line complexity--a slide line that changes its direction as it propagates, according to the stress and strain fields present. This "self-directed" (or "wandering") slide line feature will not be simple to implement. One problem is handling the changing cell layout as the slide line propagates through the grid, cutting through the middle of cells instead of merely separating adjacent cells. In principle, the finite element numbering scheme can handle such a procedure by creating new nodes wherever they are required (refer to Appendix F of reference 16), but significant new programming will be required. Another problem, and perhaps the most difficult, will be to determine the criterion that controls the direction the slide line takes. The direction of the plane of maximum shear strain would be one ingredient in this criterion, but it is clear that the physics of the problem will have to be studied more.

So far, we have discussed only nonintersecting slide lines (these are often referred to as "single" slide lines, but there may be more than one in a calculation, provided they don't intersect). But for a penetration scenario that includes a combination of penetrator deformation and removal of a plug (or any fragmented region)--and this includes almost all realistic penetrations--there is a need for intersecting or

"double" slide lines. One slide line, located within the armor plate, allows the plug to slip out from the rest of the plate. The other slide line, whose slip surfaces initially comprise the front surface of the armor plate and the impact and lateral edges of the penetrator, respectively, allows the distorting penetrator to slide with respect to the distorting target. Because both processes may occur simultaneously, and because the two slide lines intersect, one pair of nodes of one slide line will need to slip along the other line. And therein lies the complication.

We have very recently attempted a double slide line calculation with an unzipping slide line as one of two intersecting lines. It appeared to work well, but this feature needs to be tested and exercised in different geometries to complete the implementation.

Task 3: Proof Tests of the Computational Method

To determine the accuracy of our computational method for predicting penetration and fragmentation, we recommend that proof tests be performed by simulating several penetration scenarios for which adequate data exists. These scenarios should cover a reasonably wide range of impact velocity and resultant damage to exercise as many different features of the computational method as possible. But the geometries should be kept as simple as possible so that these proof tests may be performed before some of the modifications described in the first two tasks are implemented. By simulating only normal impacts, for example, we can perform the proof tests without first having to implement the self-directing slide line feature.

Two experiments performed during the current BRL program are particularly suitable for testing a wide range of computational features. Both involve the normal impact of a blunt-nosed 4340 steel rod into an RHA plate. Thus, 4340 steel ($R_c 40$) and RHA (cut from 10-cm-thick plates) are currently the materials whose shear banding kinetics have been best characterized.

One impact, at 0.792 km/s, just above the ballistic limit, resulted in the removal of a plug, but there was no other damage (except homogeneous plastic deformation) in the plug or the remainder of the armor plate (see Figure 34). The penetrator remained intact, embedded in the plug, with some shear banding damage in the impact end. The other impact, at 1.55 km/s, resulted in a large amount of downrange fragmentation from both the armor and the penetrator, mostly in the form of small fragments (see Figure 33). The region in the target plate adjacent to the penetration hole was heavily shear banded.

We recommend performing proof tests of C-HEMP and SHEAR4 by simulating the experiments described above (or other penetration experiments). It may be necessary to complete implementation of some of the modifications described in the first two tasks (the double slide line feature, for example) before performing these proof tests. Furthermore, as some of the more advanced features become implemented in C-HEMP and SHEAR4, additional proof tests will be needed (an oblique impact, for example, to test the self-directing slide line).

Finally, we recommend one other type of proof test. It relates to the use of a two-dimensional code to simulate a three-dimensional problem—the oblique impact of a rod on a plate. We plan to solve this problem with the standard planar solution: the oblique impact of a plate of infinite width upon another plate of infinite width. But we need to know how precise this approximation is, and in particular, how accurate are the final calculated results (e.g., fragment size and velocity distributions).

Such a determination can be made by comparing the results of two simulations of a set of zero-obliquity rod-into-plate impacts (such as the pair described above). One simulation would use the true axisymmetric geometry, while the other would use the planar approximation. A comparative study by Zukas³⁰ using ogival projectiles showed that the planar approximation was quite accurate at early times, but that its accuracy degraded with increasing time because it neglected such important physical phenomena as the out-of-plane motions leading to

lateral stress relaxation. We recommend performing a similar comparative study, using the blunt-nosed projectile impacts described above, to assess the accuracy of the planar approximation in oblique impact simulations with SHEAR4 and C-HEMP.

Task 4: Simplification of Computational Procedure

The ultimate goal of this effort is to develop a procedure available for routine use by both SRI and BRL (and eventually other DoD agencies) for armor and penetrator design calculations, as well as for other fragmentation applications. We recommend simplifying both the calculational models and the experimental procedures necessary to characterize a material to be modeled, without sacrificing the procedures integrity or accuracy. Below we describe various methods of effecting this simplification.

One method is to simplify the computational model for shear banding by eliminating from the nucleation, growth, or coalescence criteria those variables that do not significantly affect the outcome. These may include material parameters obtained from the characterizing experiments, as well as constants obtained from the literature. Determining which variables can be safely eliminated can be done by systematically varying the input parameters used in a series of penetration simulations and observing the effect on the final results (such as the fragment size distribution). If changes in a particular parameter have little or no effect on the final results for a wide range of impact velocities, then that parameter should be eliminated as a variable from the model. The two proof test scenarios described in Task 3 may serve as a good vehicle for these parameter variation studies.

Other methods involve simplifying the characterization procedure. Using the shear banding damage model to describe the behavior of a particular material requires determining which parameters govern the kinetics of shear banding in that material. Obtaining these parameters has been a lengthy procedure, including, in addition to standard quasi-static tensile tests (if unavailable in the literature), a series of CFC

experiments and computer simulations. The complete procedure has been done for only two materials: 4340 steel (R_c40) and an RHA. Computational simulation of scenarios for other materials would be much easier if the characterization procedure were simplified.

Simplification may take several forms. First, the number of CFC experiments to be performed may be reduced by modifying the experimental design. In the past, most CFC specimen tubes were internally loaded with a single density of explosives, and the density was varied for different experiments to obtain a wide range of shear band damage. However, in one experiment performed last year with RHA, the explosive density was varied as a function of axial position within the tube, and an adequately wide range of damage was obtained from that single experiment.

Second, the amount of data to be obtained from a series of CFC experiments may be reduced. If the parameter variation study, outlined above, has shown that a particular material parameter has a negligible effect on the simulated outcome, then that parameter need not be measured. For example, the shape of a shear band in its slip plane is obtained from CFC experiments, and in fact, a significant metallographic effort is needed just to obtain that one parameter. In the three different steels studied so far, the shape is semicircular. Substantial experimental effort can be saved if highly eccentric semi-elliptical shapes would produce a similar outcome in the computational simulations.

Also, if experimental studies of a class of materials reveal no significant variation in a particular parameter, then that parameter may not need to be measured for a new material of that class. This would be true even if varying that parameter affected the computational outcome. Using the same example as above, we may decide that all steels are likely to exhibit semicircular shear bands. There is of course a risk in doing this, but the effort saved may make the risk worthwhile.

Third, we may not need to follow the entire procedure for characterizing a new material if certain of its properties are similar to those of previously characterized materials. This simplification could

be fundamentally important. If we could identify certain material properties from which we could (perhaps in conjunction with other data) obtain shear band kinetics parameters, then we would not only have simplified the characterization process, but also increased our understanding of the shear banding phenomenon.

For example, suppose we tested a series of CFC specimen tubes that were from the same batch of steel but heat-treated to different hardnesses. Suppose also that the results indicated that certain parameters, such as shear banding nucleation rate, were identical over the range of hardness studied, while others, such as nucleation threshold strain, varied in a manner that could be related to other material variables (e.g., the dynamic yield curve). We could then hypothesize that, at least for this particular steel, the nucleation rate was an invariant of the yield curve, while the threshold strain was a particular function of the yield curve. And the hypothesis could be tested by comparison with CFC results of yet another hardness of the same specimen material. Finally, if similar results were obtained for several different materials within a particular class of materials (e.g., all steels), we could then generalize the results to all materials within that class and thus reduce further characterization efforts.

This procedure will require a significant effort and a large data base. However, we do have an appropriate data base with which to begin the procedure: CFC test data on three different hardnesses of 4340 steel. We have generated parameters for one of the hardnesses (R_c40), but have yet to complete data analysis for hardnesses R_c52 and R_c21 .

One other point should be discussed here: using alternative characterization experiments. Depending upon the results of the simplification efforts described above, CFC tests may not be the most efficient means of generating shear banding parameters for certain materials. For example, if it can be shown that for a particular steel only the shear band threshold strain and the dynamic yield curve need to be determined, using an alternative experiment, the symmetric rod impact test, would reduce the total effort. This latter test generates

a dynamic yield curve, and is also sensitive to the shear band threshold strain.

Task 5: Application of Computational Method to Various Scenarios

As the modifications described in the first four tasks are implemented and tested, the calculational method will become applicable to an ever widening variety of penetration or other fragmentation scenarios. Therefore, we recommend appropriate applications of the computational method, such as those described below.

The first such application is a study of scaling in armor penetration. Small-scale testing is widely used by armor and penetrator designers because it is time and cost efficient. It is thus very important to know how well armor penetration and the resultant fragmentation scale with size. It has been shown previously that tensile failure does not obey replica scaling laws, since the nucleation and growth of voids are rate-dependent processes.² A particular scenario that results in negligible void growth for a small-scale simulation will often show substantial void growth for a full-scale simulation.

Since the shear band nucleation and growth criteria in SHEAR3 or SHEAR4 are time-dependent in a manner similar to that for tensile voids, it is expected that shear banding would also not obey replica scaling laws. A preliminary computational study of scaling in CFC experiments³¹ showed a significant variation of shear banding for different scale factors.

A more definitive shear band scaling study, and one more directly relevant to armor penetration, would involve selecting a set of penetration scenarios that cover a wide range of impact velocities and resultant damage (the two experiments recommended in Task 3 for the proof tests would be appropriate), varying the scale factor in both experimental tests (or use existing data, if available) and computer simulations of these scenarios, and observing how closely the simulations predict the resultant damage for different scale factors. It may turn out, for example, that fragmentation scales reasonably well at high

impact velocities but that damage by simple plugging at lower velocities does not. This type of information would be of great value in planning design experiments.

Other possible applications include the following.

DU-into-RHA Penetration Studies

BRL has a large DU-into-RHA fragmentation data base, covering a wide range of velocity and obliquity, available for use in conjunction with computational studies. The simulation of previously performed DU CFC experiments must be completed to obtain a complete set of DU shear banding parameters.

Fragmentation Device Studies

The simulation of fragmentation devices has been limited by the fact that different regions fail by different mechanisms. In fragmenting shells, shear banding predominates near the interior of the shell wall, while tensile failure predominates at the exterior. This limitation will be greatly diminished once the feature (described in Task 1) is implemented that allows a computational cell to select the failure appropriate to its loading history.

Task 6: Documentation and Transfer to BRL

Maximizing the potential utility of a computational method for armor penetration can be achieved only by transferring to BRL the capability to use the method routinely. We recommend that this be done by thoroughly documenting the C-HEMP code and the failure models, and by directly assisting the specific BRL personnel who will be responsible for using the computational method.

Although C-HEMP was developed for use on SRI's VAX computer, only relatively minor modifications will be needed to make the code compatible with BRL's CDC-6600 computer. Depending upon the final size of C-HEMP, some segmentation may be required, to fit the memory space available on the BRL computer. Also, some FORTRAN statements will need to be changed for language compatibility.

REFERENCES

1. "Materials Response to Ultra-High Loading Rates," prepared by the Committee on Materials Response to Ultra-High Loading Rates of the National Materials Advisory Board, Publication NMAB-356 (National Academy of Sciences, Washington, D.C.), 1980.
2. T. W. Barbee, Jr. et al., "Dynamic Fracture Criteria for Ductile and Brittle Materials," *Journal of Materials*, JMLSA, Vol. 7, No. 3, pp. 393-401 (Sept. 1972).
3. D. A. Shockey, L. Seaman, and D. R. Curran, "Dynamic Fracture of Beryllium Under Plate Impact and Correlation with Electron Beam and Underground Test Results," SRI International Final Report No. AFWL-TR-73-12, Kirtland Air Force Base, NM (Jan. 1973).
4. D. R. Curran, D. A. Shockey, and L. Seaman, "Dynamic Fracture Criteria for a Polycarbonate," *Journal of Applied Physics*, Vol. 44, No. 9, pp. 4025-4038 (1973).
5. D. A. Shockey et al., "Fragmentation of Rock under Dynamic Loads," *International Journal of Rock Mechanics Science and Geomechanics Abstracts*, Vol. 11, pp. 303-317 (1974).
6. L. Seaman, D. R. Curran, and D. A. Shockey, "Computational Methods for Ductile and Brittle Fracture," *Journal of Applied Physics*, Vol. 47, No. 11, pp. 4814-4826 (1976).
7. D. R. Curran, L. Seaman, and D. A. Shockey, "Dynamic Failure of Solids," *Physics Today*, Vol. 30, No. 1, pp. 46-55 (Jan. 1977).
8. D. A. Shockey, D. R. Curran, and L. Seaman, "Computer Modeling of Microscopic Failure Processes Under Dynamic Loads," in High Velocity Deformation of Solids (Springer-Verlag, Berlin, 1979), proceedings of the IUTAM Symposium in Tokyo, Japan (Aug. 1977).
9. D. A. Shockey et al., "A Computational Model for Fracture of Pressure Vessel Steel Derived from Experimental Data," Paper No. 78-PVP-92, presented at the Joint ASME/CSME Pressure Vessel and Piping Conference, Montreal, Canada (June 1978).
10. L. Seaman, D. R. Curran, and D. A. Shockey, "Development of a Microfracture Model for High Rate Tensile Damage," in Creep and Fracture of Engineering Materials and Structures, Wilshire and Owens, eds., (Pineridge Press, Swansea, U.K., 1981), p. 345, proceedings of a conference held at University College, Swansea (March 1981).

11. L. Seaman et al., "Development of a Shear Band Model for Fragmentation in Exploding Cylinders," SRI International Final Report No. N00178-74-C-0450 for Naval Surface Weapons Center, Dahlgren, VA (Aug. 1974).
12. D. C. Erlich et al., "Development and Application of a Computational Shear Band Model," SRI International Final Report on Contract DAAD05-76-C-0762 for U.S. Army Ballistic Research Laboratory, Aberdeen, MD (May 1977).
13. D. C. Erlich et al., "A Preliminary Study of Armor Penetration by Shear Banding," Vol. 1 of SRI International Final Report No. DAAK11-77-C-0083 for U.S. Army Ballistic Research Laboratory, Aberdeen, MD (Aug. 1978).
14. D. C. Erlich, D. R. Curran, and L. Seaman, "Further Development of a Computational Shear Band Model," SRI International Final Report No. DAAG46-77-C-0043 for U.S. Army Materials and Mechanics Research Center, Watertown, MA (May 1979).
15. D. R. Curran et al., "Computational Model for Armor Penetration," SRI International First Annual Report No. DAAK11-78-C-0115 for U.S. Army Ballistic Research Laboratory, Aberdeen, MD and U.S. Army Materials and Mechanics Research Center, Watertown, MA (Nov. 1979).
16. D. C. Erlich et al., "Computational Model for Armor Penetration," SRI International Second Annual Report No. DAAK11-78-C-0115 for U.S. Army Ballistic Research Laboratory, Aberdeen, MD and U.S. Army Materials and Mechanics Research Center, Watertown, MA (Nov. 1980).
17. K. H. Eckelmeyer, "Aging Phenomena in Dilute Uranium Alloys," in Physical Metallurgy of Uranium Alloys, Burke et al., editors, (Brooke Hill Publishing Co., Chestnut Hill, MA, 1976), p. 463.
18. H. J. Saxton, "Fracture of Uranium Alloys," in Physical Metallurgy of Uranium Alloys, Burke et al., editors (Brooke Hill Publishing Co., Chestnut Hill, MA, 1976), p. 349.
19. H. L. Yakel, "Review of X-Ray Diffraction Studies in Uranium Alloys," in Physical Metallurgy of Uranium Alloys, Burke et al., editors (Brooke Hill Publishing Co., Chestnut Hill, MA, 1976), p. 282.
20. M. Hansen, Constitution of Binary Alloys (McGraw-Hill Book Co., Inc., New York, 1958), p. 1239.
21. A. M. Ammons, "Precipitation Hardening in Uranium-Rich Uranium-Titanium Alloys," in Physical Metallurgy of Uranium Alloys, Burke et al., editors (Brooke Hill Publishing Co., Chestnut Hill, MA, 1976), p. 532.

22. The Aerospace Structural Metals Handbook, AFML-TR-68-115, Vol. 1 (Mechanical Properties Data Center, Traverse City, MI, 1972).
23. Metals Handbook, 8th edition, Vol. 1 (American Society for Metals, Cleveland, OH, 1961), p. 1208.
24. Metals Handbook, 7th edition (American Society for Metals, Cleveland, OH, 1948), pp. 526-534.
25. R. M. Brick and A. Phillips, Structure and Properties of Alloys (McGraw-Hill Book Co., Inc., New York, NY, 1949), p. 16.
26. Metals for Supersonic Aircraft and Missiles, Proc. of Conf. on Heat Tolerant Metals for Aerodynamic Applications, Jan. 1959, University of New Mexico, Albuquerque, NM (American Society for Metals, Cleveland, OH, 1958), p. 25.
27. J. A. Gottbrath, "Mechanical Properties of Some Candidate Titanium Alloys for SST Applications," Research Report No. LR19185, Lockheed California Co., Burbank, CA (April 1968).
28. M. Linord, "Etude des Alliages Uranium--Titane a Faible Teneur en Titane en Poids," Rapport CEA-R-4180, Centre d'Etude de Valduc (July 1971).
29. D. A. Shockey et al., "[Confidential Title]," SRI International Final Report No. DNA-001-78-C-0266 for Defense Advanced Research Projects Agency, Arlington, VA (Jan. 1979). [CONFIDENTIAL]
30. J. A. Zukas et al., Impact Dynamics, (John Wiley and Sons, NY, 1982), pp. 389-391.
31. L. Seaman, D. R. Curran, and D. A. Shockey, "Scaling of Shear Band Fracture Processes," in Material Behavior Under High Stress and Ultra-high Loading Rates, Proceedings of 29th Sagamore Conference at Lake Placid, NY (July 1982).

DISTRIBUTION LIST

<u>No. of Copies</u>	<u>Organization</u>	<u>No. of Copies</u>	<u>Organization</u>
12	Administrator Defense Technical Info Center ATTN: DTIC-DDA Cameron Station Alexandria, VA 22304-6145	1	Director US Army Air Mobility Research and Development Laboratory Ames Research Center Moffett Field, CA 94035
1	HQDA (DAMA-ART-M) Washington, DC 20310	1	Commander US Army Communications - Electronics Command ATTN: AMSEL-ED Fort Monmouth, NJ 07703
1	Commander US Army Materiel Command ATTN: AMCDRA-ST 5001 Eisenhower Avenue Alexandria, VA 22333-0001	1	Commander ERADCOM Technical Library ATTN: DELSD-L (Reports Section) Fort Monmouth, NJ 07703-5301
1	Commander Armament R&D Center US Army AMCCOM ATTN: SMCAR-TSS Dover, NJ 07801	1	Commander US Army Missile Command Research, Development and Engineering Center ATTN: AMSMI-RD Redstone Arsenal, AL 35898
1	Commander Armament R&D Center US Army AMCCOM ATTN: SMCAR-TDC Dover, NJ 07801	1	Director US Army Missile & Space Intelligence Center ATTN: AIAMS-YDL Redstone Arsenal, AL 35898-5500
1	Commander US Army Material Technology Laboratory ATTN: John Mescall Watertown, MA 02172	1	Commander US Army Tank-Automotive Command ATTN: AMSTA-TSL Warren, MI 48397-5000
1	Director Benet Weapons Laboratory Armament R&D Center US Army AMCCOM ATTN: SMCAR-LCB-TL Watervliet, NY 12189	3	Director US Army TRADOC Systems Analysis Activity ATTN: ATAA-SL White Sands Missile Range, NM 8002
1	Commander US Army Armament, Munitions and Chemical Command ATTN: SMCAR-ESP-L Rock Island, IL 61299	1	Commandant US Army Infantry School ATTN: ATSH-CD-CSO-OR Fort Benning, GA 31905
1	Commander US Army Aviation Research and Development Command ATTN: AMSAV-E 4300 Goodfellow Blvd St. Louis, MO 63120		

DISTRIBUTION LIST

<u>No. of Copies</u>	<u>Organization</u>	<u>No. of Copies</u>	<u>Organization</u>
1	Commander US Army Development & and Employment Agency ATTN: MODE-TED-SAB Fort Lewis, WA 98433	10	Central Intelligence Agency Office of Central Reference Dissemination Branch Room GE-47 HQS Washington, DC 20502
1	AFWL/SUL Kirtland AFB, FL 87117		<u>Aberdeen Proving Ground</u>
1	AFATL/DLODL Eglin AFB, FL 32542-5000		Dir, USAMSAA ATTN: AMXSY-D AMXSY-MP (H. Cohen)
1	AFATL (Joe Foster) Eglin AFB, FL 32452-5000		Cdr, USATECOM ATTN: AMSTE-TO-F
2	US Army Research Office ATTN: George Mayer Robert Singleton P. O. Box 12211 Research Triangle Park, NC 27709		Cdr, CRDC, AMCCOM ATTN: SMCCR-RSP-A SMCCR-MU SMCCR-SPS-IL
2	Naval Surface Weapons Center ATTN: William H. Holt Willis Mock, Jr. Dahlgren, VA 22448		
1	Naval Research Laboratory ATTN: Rick Mako Washington, DC 20375		

USER EVALUATION SHEET/CHANGE OF ADDRESS

This Laboratory undertakes a continuing effort to improve the quality of the reports it publishes. Your comments/answers to the items/questions below will aid us in our efforts.

1. BRL Report Number _____ Date of Report _____

2. Date Report Received _____

3. Does this report satisfy a need? (Comment on purpose, related project, or other area of interest for which the report will be used.) _____

4. How specifically, is the report being used? (Information source, design data, procedure, source of ideas, etc.) _____

5. Has the information in this report led to any quantitative savings as far as man-hours or dollars saved, operating costs avoided or efficiencies achieved, etc? If so, please elaborate. _____

6. General Comments. What do you think should be changed to improve future reports? (Indicate changes to organization, technical content, format, etc.) _____

CURRENT ADDRESS Name _____
 Organization _____
 Address _____
 City, State, Zip _____

7. If indicating a Change of Address or Address Correction, please provide the New or Correct Address in Block 6 above and the Old or Incorrect address below.

OLD ADDRESS Name _____
 Organization _____
 Address _____
 City, State, Zip _____

(Remove this sheet, fold as indicated, staple or tape closed, and mail.)

FOLD HERE

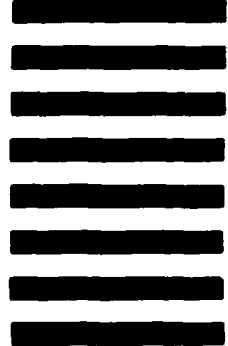
Director
US Army Ballistic Research Laboratory
ATTN: DRXBR-OD-ST
Aberdeen Proving Ground, MD 21005-5066



NO POSTAGE
NECESSARY
IF MAILED
IN THE
UNITED STATES

OFFICIAL BUSINESS
PENALTY FOR PRIVATE USE: \$300

BUSINESS REPLY MAIL
FIRST CLASS PERMIT NO 12062 WASHINGTON, DC
POSTAGE WILL BE PAID BY DEPARTMENT OF THE ARMY



Director
US Army Ballistic Research Laboratory
ATTN: DRXBR-OD-ST
Aberdeen Proving Ground, MD 21005-9989

FOLD HERE

END

DATE

FILMED

4-88

DTIC